Law of incipient separation for turbulent flows over airfoils as inferred by RANS

Shao-Chi Huang

A thesis

submitted in partial fulfillment of the

requirements for the degree of

Master of Science in Aeronautics and Astronautics

University of Washington

2021

Reading Committee:

Antonino Ferrante, Chair

Owen Williams

Program Authorized to Offer Degree:

College of Engineering,
William E. Boeing Department of Aeronautics and Astronautics

University of Washington

Abstract

Law of incipient separation for turbulent flows
over airfoils as inferred by RANS

Shao-Chi Huang

Chair of the Supervisory Committee:
Associate Professor Antonino Ferrante
Aeronautics and Astronautics

In a recent study, Lu, Aithal & Ferrante (*AIAA J.*, 2021) have discovered the law of incipient separation for curved ramps that predicts the incipiency of flow separation by knowing only a few geometrical parameters of the ramp and the Reynolds number of the incoming flow. In the present study, we have searched for a similar law to predict the separation of the turbulent flow over airfoils. With that goal, we have conducted two-dimensional Reynolds averaged Navier-Stokes (RANS) wall-resolved simulations of incompressible turbulent flows over several airfoils over a range of angles of attack, α. Along the study, we have carried out verification and validation of RANS using the Spalart-Allmaras model against the experimental measurements by Wadcock (*NASA-CR*-177450, 1987) for the turbulent flow over a NACA4412 airfoil at a Reynolds number based on the airfoil chord length of $Re_c = 1.64 \times 10^6$. From such comparison, we have found that although the RANS prediction fails when the airfoil approaches its maximum lift ($\alpha \geq 12°$), the incipient separation occurs at a much smaller angle of attack, i.e., $\alpha \simeq 1°$. Thus, we have investigated the effects of the angle of attack, airfoil thickness, and camber on the incipiency of flow separation for eleven different airfoils and $Re_c \in [1.64 \times 10^6, 6 \times 10^6]$. From the RANS results, we have determined a law for predicting the incipiency of turbulent flow separation that relies only on a few key airfoil's geometrical parameters, angle of attack and the Reynolds number of the flow.

TABLE OF CONTENTS

LIST OF FIGURES

LIST OF TABLES

NOMENCLATURE

Upper-case Roman

C_f = local skin-friction coefficient ($= 2\tau_w/\rho U_\infty^2$)

C_p = local pressure coefficient ($= 2(p - p_{\text{ref}})/\rho U_\infty^2$)

H = shape factor

L_d = downstream domain length normalized by the airfoil chord length, c

L_u = upstream domain length normalized by the airfoil chord length, c

N_{A} = number of grid points over the airfoil

N_i = number of grid points in ξ direction

N_j = number of grid points in η direction

N_{LT} = number of grid points from the airfoil leading edge to trailing edge

N_{wake} = number of grid points in the wake

P = point of maximum y, $y_{\max}$, of airfoil

P = source term for grid generation

P_{o} = source term for grid orthogonality

P_{s} = source term for grid stretching

Q = source term for grid generation

Q_{o} = source term for grid orthogonality

Q_{s} = source term for grid stretching

Re_c = Reynolds number ($= \rho U_\infty c/\mu$)

U = velocity, m/s

Lower-case Roman

a_s = grid stretching coefficient

b_{ij} = blending function

c = airfoil chord length, m

c_s = grid stretching coefficient

g_{ab} = metric tensor

g_{o11} = g_{11} of metric tensor evaluated at $j = 1$

g_{o22} = g_{22} of metric tensor evaluated at $j = 1$

h = airfoil maximum thickness normalized by the airfoil chord length, c

h_c = airfoil maximum camber normalized by the airfoil chord length, c

m_{P} = characteristic slope ($= |\Delta x_{\mathrm{P}}/\Delta y_{\mathrm{P}}|$)

$m_{\mathrm{P}_{\alpha 0}}$ = characteristic slope at $\alpha = 0$

$\tilde{m}_{\mathrm{P}}$ = modified characteristic slope, m_{P}, (Eq. (4.4))

n = wall-normal direction

p = gauge pressure (static), Pa

x = Cartesian coordinate in the streamwise direction, normalized by the airfoil chord length, c

x_{P} = x of point P

$x_{\mathrm{P}_{\alpha 0}}$ = x of point P at $\alpha = 0$

y = Cartesian coordinate vertical to the streamwise direction, normalized by the airfoil chord length, c

y_{P} = y of point P

$y_{\mathrm{P}_{\alpha 0}}$ = y of point P at $\alpha = 0$

Upper-case Greek

$\tilde{\Gamma}$ = modified parameter including to airfoil geometric features, (Eq. (4.3))

Δx_{P} = x-distance between point P and airfoil trailing edge normalized by the chord length, c

Δy_{P} = y-distance between point P and airfoil trailing edge normalized by the chord length, c

Lower-case Greek

α = angle of attack, deg

α_{m} = g_{22} of metric tensor, g

β_{m} = g_{12} of metric tensor, g

γ_{a} = grid stretching constant for airfoil profile

γ_{j} = grid stretching constant for η direction near the airfoil for $j = 1$

γ_{m} = g_{11} of metric tensor, g

γ_{wake} = grid stretching constant for airfoil wake in the ξ direction

γ_{Q} = grid stretching constant for source term Q

δ_{b} = positive constant for blending function

δ_{m} = determinant of metric tensor, g

ϵ = relative change

η = Cartesian coordinate vertical to streamwise direction of generalized-coordinates space

θ = angle in quadrilateral cell

μ_t = eddy viscosity

ν = kinematic viscosity, m^2/s

ν_t = turbulent viscosity, m^2/s

$\tilde{\nu}$ = modified turbulent viscosity, m^2/s

ξ = Cartesian coordinate in streamwise direction of generalized-coordinates space

ρ = density, kg/m^3

σ = L_2 norm of the deviation from law of incipient separation

$\bar{\sigma}$ = Normalized L_2 norm of the deviation from law of incipient separation

τ_w = wall shear stress, N/m^2

Subscripts

d = downstream

i = inlet, computational domain index, or direction index $i = 1, 2, 3$

j = computational domain index

o = outlet

u	=	upstream
w	=	wall
avg	=	average
crit	=	critical
max	=	maximum value
min	=	minimum value
ref	=	reference
sep	=	separation
∞	=	free-stream

ACKNOWLEDGMENTS

I would like to thank Professor Ferrante and Professor Williams for their support and guidance in the process of achieving my Master's degree.

Second, I would like to thank Abhiram Aithal for his mentorship throughout my research.

Lastly, the support of my friends and family. I feel lucky to have you with me during these trying times.

This work was facilitated though the use of advanced computational, storage, and networking infrastructure provided by the Hyak supercomputer system at the University of Washington, Seattle.

DEDICATION

to my dear wife, Caroline

Chapter 1

INTRODUCTION

Flow separation over airfoils affects the airfoil lift and drag coefficients. Therefore, the prediction of flow separation is an important topic for aerodynamic design. As the angle of attack increases for an airfoil, the adverse pressure gradient (APG) over the airfoil suction surface gets stronger, and may lead to flow separation. The phenomenon can be observed by the zero-velocity gradient in the wall-normal direction at the separation point on the airfoil surface and the reversed streamwise flow direction after the separation point.

Experiments and CFD modeling have been conducted for turbulent flow over airfoils that may undergo flow separation, e.g. [4, 5, 8, 9, 12, 13, 24, 27]. Counsil [9] used RANS to study the flow separation at $Re_c \in [4.8\times10^4, 2.5\times10^5]$ for NACA0012 and SD7003 airfoils. Boutilier [4] showed experimentally that, as the angle of attack was increased, the point of separation for the NACA0018 airfoil at $Re_c = 1 \times 10^5$ moved closer to the airfoil leading edge. Further, Wadcock [27] studied the C_p distribution over the NACA4412 airfoil at $Re_c = 1.64 \times 10^6$ at various angles of attack both before and after flow separation, and showed that as the airfoil approaches its maximum lift ($\alpha \geq 12^\circ$), the pressure coefficient became almost constant after the separation point. Cole and Wadcock [8] studied experimentally, the flow field over the trailing edge of the NACA4412 airfoil at $Re_c = 1.5 \times 10^6$. Many researchers have proposed various methods to predict flow separation, namely, Stratford's method [24], Goldschmied method [12], Head's method [13] and Cebeci-Smith method [5]. Stratford's method [24] for turbulent flows requires the knowledge of the pressure coefficient along the airfoil, C_p. Goldschmied [12], on the other hand, defines the separation criterion based on the skin-friction coefficient, C_f, of the minimum pressure point. Head's method [13] is an integral method that takes into account the shape factor, H, of the boundary layer, and the Cebeci-

Smith method [5] requires solving a differential equation and defined eddy viscosity, μ_t, as a function of the local boundary layer velocity profile. All the methods mentioned above, however, require *a priori* information of the flow field within the boundary layer to predict flow separation, e.g., $C_p(x)$ or H.

In a recent study, Lu, Aithal & Ferrante [16] have discovered a criterion for flow separation over a curved ramp that depends only on the maximum slope and height-to-length ratio of the ramp, and inflow Reynolds number. In that spirit, in the present work, we aim to answer the following question regarding flow separation over airfoils: "Is there an analogous law of incipient separation for airfoils that depends only on knowing a few key parameters related to the airfoil geometry, angle of attack, and flow properties of the incoming flow?"

To answer this question, we have first verified the configurations of the RANS simulations over airfoils with respect to the computational domain size, boundary conditions, and grid resolution (Ch. 2). Second, we have validated the RANS simulations against the experimental measurements by [27] (Ch. 3). Finally we have derived a law of incipient separation for turbulent flows over airfoils which relies only on the key geometrical features of the airfoil and the Reynolds number of the flow (Ch. 4).

Chapter 2

MATHEMATICAL MODELING

2.1 Governing equations

The RANS equations for incompressible flows are

$$\frac{\partial}{\partial x_i}\langle U_i\rangle = 0, \tag{2.1}$$

$$\frac{\partial}{\partial t}\langle U_i\rangle + \langle U_j\rangle \frac{\partial}{\partial x_j}\langle U_i\rangle = -\frac{1}{\rho}\frac{\partial}{\partial x_i}\langle p\rangle + \frac{\partial}{\partial x_j}\left[(\nu+\nu_t)\frac{\partial}{\partial x_j}\langle U_i\rangle\right], \tag{2.2}$$

where $\langle U_i\rangle$ $(i = 1, 2, 3)$ are the fluid mean velocity components in the three spatial directions, p is the gauge pressure, ρ is the density, ν and ν_t are the kinematic and turbulent viscosity, respectively. In this study, the turbulent viscosity is obtained by solving one or two transport equations depending on the turbulence model. We adopted the one-equation model of Spalart-Allmaras (SA-RC) [23] and the two-equation model of Menter shear-stress transport (SST-RC) [18], both with curvature correction [21, 22]. The RANS and transport equations are solved using the commercial CFD software ANSYS Fluent [17] in two-dimensional domains, i.e., only for $i = 1, 2$ in Eqs. (2.1) and (2.2), since the present study is conducted for airfoils that do not change in the spanwise direction. Adopting 2D RANS allows us to perform numerous numerical simulations in order to investigate the existence of the law of incipient separation for turbulent flows over airfoils.

2.1.1 Boundary conditions

Fig. 2.1 shows the schematic of the boundaries of the computational domain where we impose the following boundary conditions to simulate the flow over airfoils.

Inlet: At the inlet, a uniform velocity profile is prescribed since the farfield flow does not interact with any walls before it reaches the airfoil, and for pressure, a Dirichlet boundary

condition is applied with gauge pressure, $p = 0$ Pa.

Outlet. At the outlet, the two velocity components are linearly extrapolated from their values at the interior points of the computational domain next to the outlet and for pressure, a Dirichlet boundary condition is applied with gauge pressure, $p = 0$ Pa.

Wall. At the wall, for the velocity, the no-slip boundary condition is imposed, and a Neumann boundary condition is imposed for pressure in the normal direction, n.

2.2 Computational domain

The schematic of the computational domain is shown in Fig. 2.1. The computational domain is set up as a C-grid with the domain size normalized by the airfoil chord length, c. In Fig. 2.1, L_u denotes the radius of the inlet semi-circle with the origin at the airfoil trailing edge, and L_d denotes the distance from the airfoil trailing edge to the outlet. The NACA0012 airfoil, plotted in Fig. 2.1, is used for the verification study reported in Ch. 3.1.

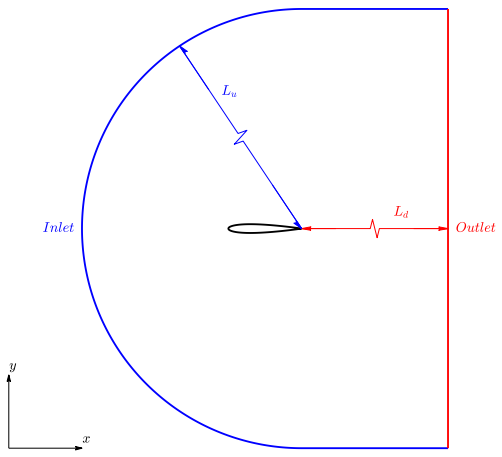

Figure 2.1: Computational domain

2.2.1 Grid generation: method

A structured grid is employed in all the simulations, and the C-grid topology is chosen to improve the orthogonality of the grid around the airfoil trailing edge. The computational grid of the physical space (x, y) in Fig. 2.2, is mapped into a uniform Cartesian grid of the rectangular domain in the generalized-coordinates space (ξ, η). i and j represent the grid indexes in the ξ and η directions, respectively. Fig. 2.2 shows the structured C-grid over a NACA0012 airfoil that was generated by our elliptic wall-normal C-grid Generator (EWN-CGrid) with $N_i = 515$, and $N_j = 129$, where N_i and N_j are the number of grid points in the ξ and η directions. The colors blue, green, magenta, and red indicates the grid lines $i = 1$, $i = N_i$, $j = 1$, and $j = N_j$, respectively.

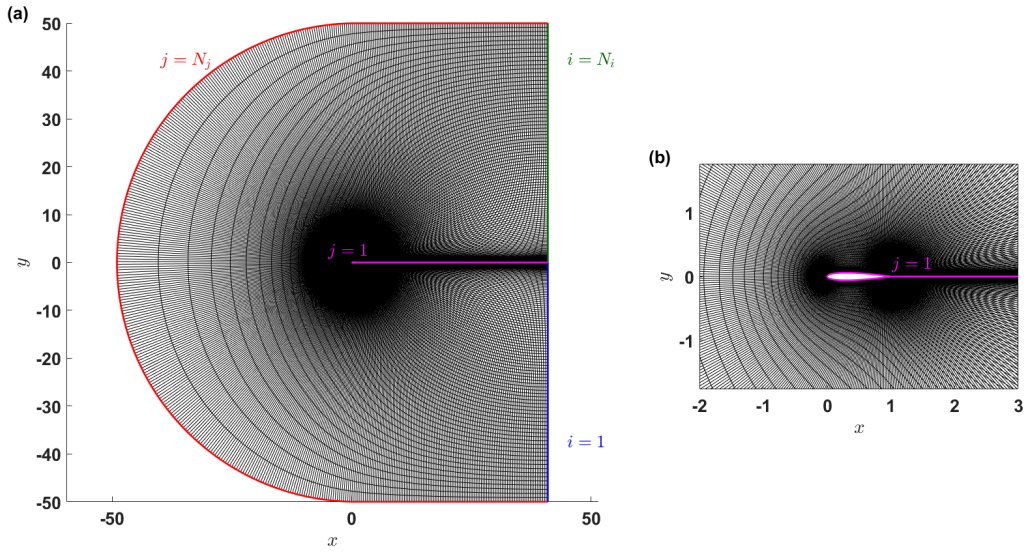

Figure 2.2: Computational grid over the NACA0012 airfoil with $N_i = 515$, and $N_j = 129$, generated by our elliptic wall-normal C-grid (EWN-CGrid) generator: (a) entire C-grid with the colors blue, green, magenta, and red indicating the grid lines $i = 1$, $i = N_i$, $j = 1$, and $j = N_j$, respectively, (b) $j = 1$ grid line showing airfoil profile and part of the wake line.

In the ξ direction, $i = 1$ and $i = N_i$ denote, respectively, the lower $(y < 0)$ and upper $(y > 0)$ lengths of the outlet boundary of the domain, while in the η direction, $j = 1$

denotes the airfoil (wall boundary) and the wake line from the trailing edge to the outlet ($x = L_d, y = 0$), and $j = N_j$ is the inlet boundary. In order to generate a C-grid over the airfoil, we have modified the method described by Thompson [26] by combining the source terms of grid stretching and grid orthogonality, and by applying a blending function to the orthogonal source terms in order to impose orthogonality of the grid in the boundary layer, near the surface of the airfoil. The computational grid (x, y), e.g., Fig. 2.2, is obtained as numerical solution of the following system of elliptic PDEs [11]:

$$\begin{aligned} \alpha_{\mathrm{m}}\frac{\partial^2 x}{\partial \xi^2} - 2\beta_{\mathrm{m}}\frac{\partial^2 x}{\partial \xi \partial \eta} + \gamma_{\mathrm{m}}\frac{\partial^2 x}{\partial \eta} + \delta_{\mathrm{m}}\left(P(\xi,\eta)\frac{\partial x}{\partial \xi} + Q(\xi,\eta)\frac{\partial x}{\partial \eta}\right) = 0, \\ \alpha_{\mathrm{m}}\frac{\partial^2 y}{\partial \xi^2} - 2\beta_{\mathrm{m}}\frac{\partial^2 y}{\partial \xi \partial \eta} + \gamma_{\mathrm{m}}\frac{\partial^2 y}{\partial \eta} + \delta_{\mathrm{m}}\left(P(\xi,\eta)\frac{\partial y}{\partial \xi} + Q(\xi,\eta)\frac{\partial y}{\partial \eta}\right) = 0, \end{aligned} \tag{2.3}$$

where $P(\xi, \eta)$ and $Q(\xi, \eta)$ are the source terms used to control interior grid behavior, $\alpha_{\mathrm{m}} = g_{22}$, $\beta_{\mathrm{m}} = g_{12}$, $\gamma_{\mathrm{m}} = g_{11}$, and $\delta_{\mathrm{m}} = g$, is the determinant of the metric tensor, g_{ab}, defined as

$$g_{ab} = \sum_{k=1}^{2} \frac{\partial x^k}{\partial \xi^a}\frac{\partial x^k}{\partial \xi^b}, \tag{2.4}$$

where $x^k =$ or x or y for $k = 1$ or 2, and $\xi^a = \xi$ or η for $a = 1$ or 2, respectively. For simplicity, the uniform Cartesian grid is chosen with $\Delta\xi = \Delta\eta = 1$, and the system of PDEs, Eq. (2.3), is discretized using the second-order central difference scheme. The source terms, $P(\xi, \eta)$ and $Q(\xi, \eta)$, in Eq. (2.3) are computed as the combination of the grid stretching source terms, P_s and Q_s, and orthogonality source terms, P_{o} and Q_{o}. In discretized form, the source terms can be written as,

$$\begin{aligned} P_{i,j} &= P_{s\ i,j} + b_{ij}P_{\mathrm{o}\ i,j}, \\ Q_{i,j} &= Q_{s\ i,j} + b_{ij}Q_{\mathrm{o}\ i,j}, \end{aligned} \tag{2.5}$$

where i and j denote the grid indexes, b_{ij} is a blending function computed as [25],

$$b_{ij} = e^{-\frac{1}{\delta_b}\frac{N_j - j}{N_j}}. \tag{2.6}$$

where, δ_b is a positive constant chosen such that the condition of grid orthogonality imposed at the airfoil boundary stays within the boundary layer. In the EWN-CGrid generater, our

method of applying the blending function differs from [25], such that by only applying the blending function to the orthogonal source terms, we are able to maintain the grid stretching near the airfoil while improving the othogonality at the boundary.

The grid stretching source terms P_s and Q_s are defined as:

$$P_{s\ i,j} = 0, \tag{2.7a}$$

$$Q_{s\ i,j} = -a_s \mathrm{sgn}(j-1) e^{-c_s|j-1|}, \tag{2.7b}$$

where $a_s = 2\times10^{11}$ and $c_s = 0.25$ are grid stretching coefficients, and sgn is the sign function. For $Q_{s\ i,j}$ with its i index in the wake, the $Q_{s\ i,j}$ is multiplied by a hyperbolic tangent function to reduce the effect of grid stretching as the grid point approaches the outlet. The $Q_{s\ i,j}$ is modified as,

$$Q_{s\ i,j} = -a_s \mathrm{sgn}(j-1) e^{-c_s|j-1|} \left[1 - \frac{\tanh(\gamma_{\text{wake}}(N_{\text{wake}} - i))}{\tanh(\gamma_{\text{wake}}(N_{\text{wake}} - 1))}\right], \tag{2.8}$$

where $\gamma_{\text{wake}} = 0.042$ is the constant which determines the degree of grid stretching and the N_{wake} represents the number of grid points in the wake. The orthogonality source terms P_{o} and Q_{o} are defined as,

$$\begin{aligned} P_{\text{o}\ i,j} = &- \frac{0.5(x_{i+1,1} - x_{i-1,1})(x_{i+1,1} - x_{i,1} + x_{i-1,1}) + 0.5(y_{i+1,1} - y_{i-1,1})(y_{i+1,1} - y_{i,1} + y_{i-1,1})}{g_{\text{o}11\ i}} \\ &- \frac{0.5(x_{i+1,1} - x_{i-1,1})(x_{i,2} - x_{i,1} + x_{i,0}) + 0.5(y_{i+1,1} - y_{i-1,1})(y_{i,2} - y_{i,1} + y_{i,0})}{g_{\text{o}22\ i}}, \end{aligned} \tag{2.9a}$$

$$\begin{aligned} Q_{\text{o}\ i,j} = &- \frac{(x_{i,2} - x_{i,1})(x_{i,2} - x_{i,1} + x_{i,0}) + (y_{i,2} - y_{i,1})(y_{i,2} - y_{i,1} + y_{i,0})}{g_{\text{o}22\ i}} \\ &- \frac{(x_{i,2} - x_{i,1})(x_{i+1,1} - x_{i,1} + x_{i-1,1}) + (y_{i,2} - y_{i,1})(y_{i+1,1} - y_{i,1} + y_{i-1,1})}{g_{\text{o}11\ i}}, \end{aligned} \tag{2.9b}$$

where $g_{\text{o}11}$ and $g_{\text{o}22}$ are, respectively, the g_{11} and g_{22} terms of the metric tensor, g, calculated

for $j = 1$ as,

$$g_{\mathrm{o11}\ i} = (x_{i+1,1} - x_{i-1,1})^2 + (y_{i+1,1} - y_{i-1,1})^2, \tag{2.10a}$$

$$g_{\mathrm{o22}\ i} = \left(\frac{0.25(y_{i+1,1} - y_{i-1,1})^2 (x_{i,2} - x_{i,1}) - 0.25(x_{i+1,1} - x_{i-1,1})(y_{i+1,1} - y_{i-1,1})(y_{i,2} - y_{i,1})}{\sqrt{g_{\mathrm{o11}\ i}}} \right)^2 + \left(\frac{-0.25(x_{i+1,1} - x_{i-1,1})(y_{i+1,1} - y_{i-1,1})(x_{i,2} - x_{i,1}) + 0.25(x_{i+1,1} - x_{i-1,1})^2 (y_{i,2} - y_{i,1})}{\sqrt{g_{\mathrm{o11}\ i}}} \right)^2. \tag{2.10b}$$

The initial conditions that were applied to the EWN-CGrid are:
For grid points over the airfoil, $N_{\mathrm{wake}} < i \leq N_{\mathrm{wake}} + N_{\mathrm{A}}$ and $j = 1$, with N_{A} representing the number of grid points over the airfoil, the grid points are defined by a double sided stretching function [1] with grid clustering near the airfoil's leading edge and trailing edge. The grid stretching has been created via mapping the uniform computational grid ξ into its non-uniform counterpart x using the hyperbolic tangent function,

$$x_i = 0.5 \left(1 - \frac{\tanh(\gamma_{\mathrm{a}}[(N_{\mathrm{LT}} - 1)/2 - i + 1])}{\tanh(\gamma_{\mathrm{a}}(N_{\mathrm{LT}} - 1)/2)} \right), \tag{2.11}$$

where $\gamma_{\mathrm{a}} = 0.055$ is the constant which determines the degree of grid stretching, and N_{LT} represents the number of grid points from the airfoil leading edge to trailing edge. Eq. (2.11) generates grid points between $x \in [0, 1]$, with clustering of grid points near $x = 0$ and $x = 1$. The y value is then determined by implementing the NACA equations using the x spacing. For grid points with the same i index as the airfoil grid points, $N_{\mathrm{wake}} < i \leq N_{\mathrm{wake}} + N_{\mathrm{A}}$, the grid points are located on the semi-circle centered at the airfoil trailing edge for $j = N_j$. The grid is stretched in the η direction, using the hyperbolic tangent function as [10],

$$x_{i,j} = (x_{i,N_j} - x_{i,1}) \left[1 - \frac{\tanh(\gamma_{\mathrm{j}}(N_j - j))}{\tanh(\gamma_{\mathrm{j}}(N_j - 1))} \right], \tag{2.12}$$

where $\gamma_{\mathrm{j}} = 0.075$. The y values are then solved based on the slope of the orthogonal line to the airfoil formed by grid points at $j = 1$ and $j = N_j$ and the x value of the same indexes.

The closest grid point to the wall in wall units is at $y^+_{\min} < 0.4$ as defined in [16]. With grid stretching in the η direction implemented as an initial condition, the convergence of the solution is more easily achieved where we decrease the chance of overlapping grid lines during iterations.

For $i \leq N_{\text{wake}}$ and $i > N_{\text{wake}} + N_{\text{A}}$, the initial condition of grid points are also determined using the hyperbolic tangent function, however, with grid stretching is in the ξ direction:

$$x_{i,j} = (x_{N_i,j} - x_{N_{\text{wake}}+1,j}) \left[1 - \frac{\tanh(\gamma_{\text{wake}}(N_{\text{wake}} - i + 1))}{\tanh(\gamma_{\text{wake}} N_{\text{wake}})}\right] + x_{N_{\text{wake}}+1,j}, \tag{2.13}$$

where $\gamma_{\text{wake}} = 0.042$ and the N_{wake} represents the number of grid points in the wake. The y values in the wake are determined by the y value of the of the same j indexes at $i = N_{\text{wake}}+1$ for $y < 0$, and $i = N_{\text{wake}} + N_{\text{af}}$ for $y > 0$.

The boundary conditions that were applied for solving Eq. 2.3 in their discretized form are:

For $i = 1$ to $i = N_i$ and $j = 1$, the Dirichlet boundary conditions are applied by specifying the profile of the airfoil and grid points in the wake.

For $i = 1$ and $j = 2$ to $j = N_j$, the Neumann-Dirichlet boundary conditions are applied with specified x location and the y location based on grid interior, $x = L_d$ and $y = y|_{i=2}$.

For $i = N_i$ and $j = 2$ to $j = N_j$, the Neumann-Dirichlet boundary conditions are applied with specified x location and the y location based on grid interior, $x = L_d$ and $y = y|_{i=N_i-1}$.

For $i < N_{\text{wake}} + 1$ and $j = N_j$, the Neumann-Dirichlet boundary conditions are applied with specified y, and x based on grid interior, $y = -L_u$, and $x = x|_{j=N_j-1}$.

For $N_{\text{wake}} < i \leq N_{\text{wake}} + N_{\text{A}}$ and $j = N_j$, the Neumann boundary conditions are applied, where grid points remains on the semi circle centered at $(x, y) = (1, 0)$ with a radius of L_u, but grid lines are kept orthogonal to the boundary.

For $i > N_{\text{wake}} + N_{\text{A}}$ and $j = N_j$, the Neumann-Dirichlet boundary conditions are applied with specified y, and x based on grid interior, $y = L_u$, and $x = x|_{j=N_j-1}$.

We solve the discretized system by successive overrelaxation (SOR) and the convergence criterion of reaching 10^{-6} for the grid solution. The source terms P_s, Q_s, P_{o}, and Q_{o} are all

evaluated and updated with every iteration to achieve the ideal grid such that the RANS computes the velocity profile in the viscous sublayer ($y^+ < 5$) and, thus, the wall shear-stress is computed directly from the RANS solution without using any wall-function models. The friction velocity, which is necessary to compute the viscous length scale and, then, the location of the closest grid point to the wall in wall units for this grid generation phase, has been determined by solving the "friction law" (Eq. (A.6) of [10]).

2.2.2 Grid generation: results

We have compared the grid generated with the modified Thompson's method described in Ch. 2.2.1, EWN-CGrid, with the structured grid generated by the ANSYS grid generator of Fluent. In Fig. 2.3, the Fluent grid and the EWN-CGrid over a NACA0012 airfoil with $N_i = 515$, and $N_j = 129$ are compared in a zoomed-in view. The Fluent grid (Fig. 2.3a) shows clustering of grid points along the horizontal line $y = 0$, the airfoil's surface, and the vertical line $x = 1$ at the trailing edge of the airfoil. While the EWN-CGrid (Fig. 2.3b) shows that the grid clustering is kept where needed near the airfoil's surface to resolve the boundary layer, and in the wake, and the cell's area is much more gradually changing throughout the domain than for the Fluent grid. The property of orthogonality of the Fluent grid is not satisfied particularly near the airfoil's surface where the grid lines form angles closer to 45° rather than 90°. The EWN-CGrid, on the other hand, shows that the grid lines are kept perpendicular to the airfoil and then the angles formed by the grid lines away from the airfoil in the domain vary smoothly. Fig. 2.4 shows a further detailed comparison of the two grids in zoomed in regions near the leading and trailing edges of the airfoil. Although there is grid points clustering in these regions for both grids, the Fluent grid (Fig. 2.4a) misrepresents the airfoil's surface near the leading edge, while the EWN-CGrid (Fig. 2.4b) captures it smoothly. This is due to the way the EWN-CGrid fixes the airfoil's grid points from the NACA airfoil analytical function as initial conditions and keeps them fixed as the grid generator iteratively smooths the grid points position in the interior of the domain. Near the trailing edge, the comparison of the two grids, in Figs. 2.4c and 2.4d, shows again the difference in the way

orthogonality is satisfied. A quantitative comparison of the two grids is given in Table 2.1, for the skewness, aspect ratio, and growth rate in the i and j varying index. The skewness of each quadrilateral cell is defined by the angles inside each cell:

$$\text{skewness} = \max\left(\frac{\theta_{\max} - 90}{90}, \frac{90 - \theta_{\min}}{90}\right), \tag{2.14}$$

where $\theta_{\max}$ and $\theta_{\min}$ are the largest and smallest angle inside each cell. For a rectangular cell, i.e., $\theta_{\max} = \theta_{\min} = 90°$, the skewness, Eq. (2.14), is then zero.

The aspect ratio of each cell is defined as the ratio of the longest to shortest length of the quadrilateral sides. The growth rate calculation along the i or j varying grid lines is the ratio of the distance between successive grid points in the ξ or η direction. From Table 2.1, the skewness of the Fluent grid in the viscous sublayer ($y^+ < 5$) is 0.78, which is more than two times larger than the skewness of EWN-CGrid of 0.38. For the aspect ratio, both the grids show high aspect ratio due to the stretching of the grid points near the airfoil, however, the Fluent grid's max aspect ratio is three times larger than that of the EWN-CGrid. Both grids have an averaged growth rate in the viscous sublayer smaller than 1.3, as recommended in [20]. The $y^+_{\min}$ is kept below the value of 0.4 described in [16] in order to maintain a wall-resolved grid. The average growth rate along the i index varying line for the Fluent grid is 26 which is about twelve times larger than that of the EWN-CGrid. In summary, the qualitative (Figs. 2.3 and 2.4) and quantitative (Table. 2.1) comparisons of the two grids show a significant improvement from the Fluent grid to the EWN-CGrid.

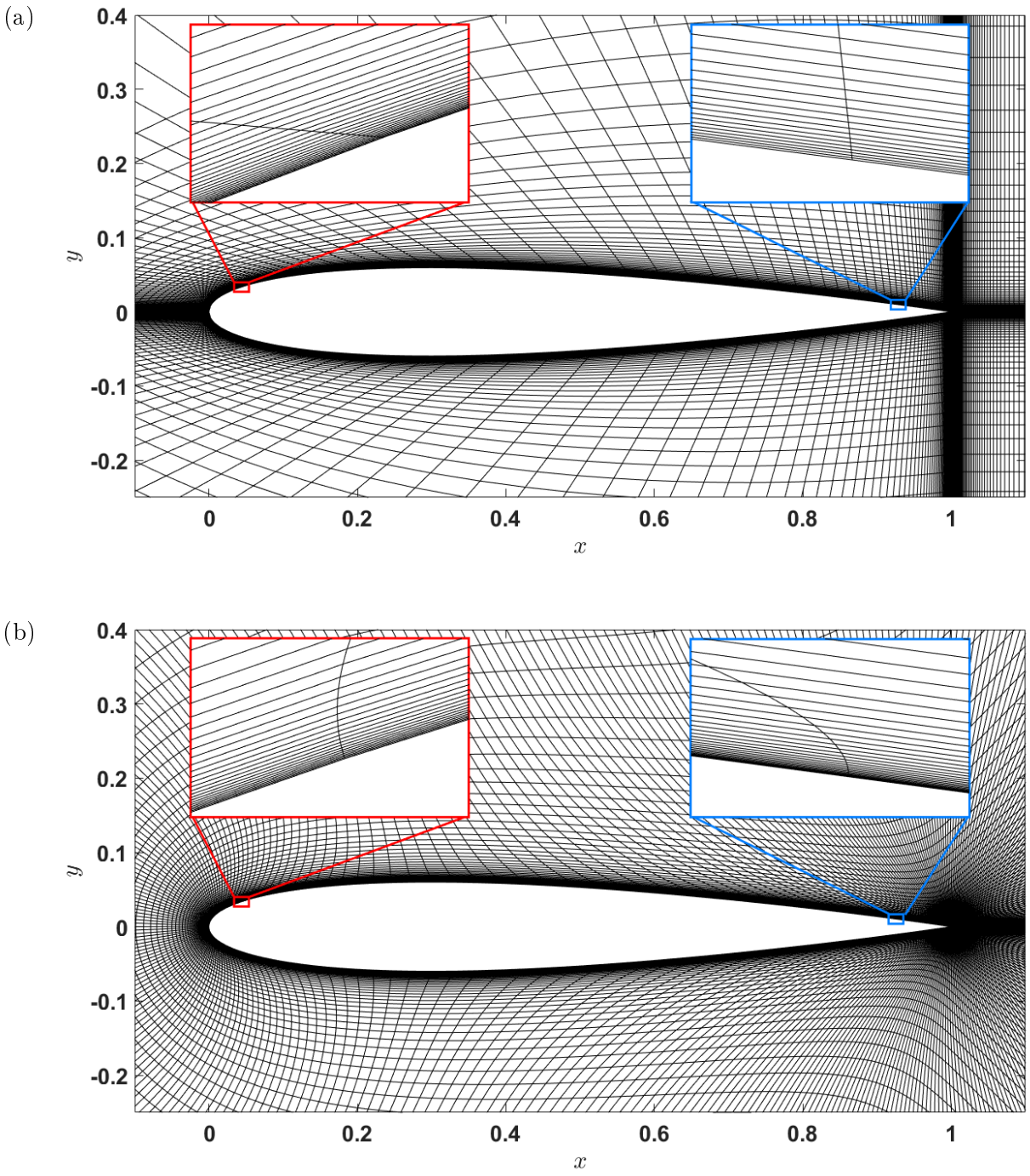

Figure 2.3: Grid comparison over a NACA0012 airfoil using 515×129 grid points: (a) ANSYS Fluent structured grid, (b) EWN-CGrid.

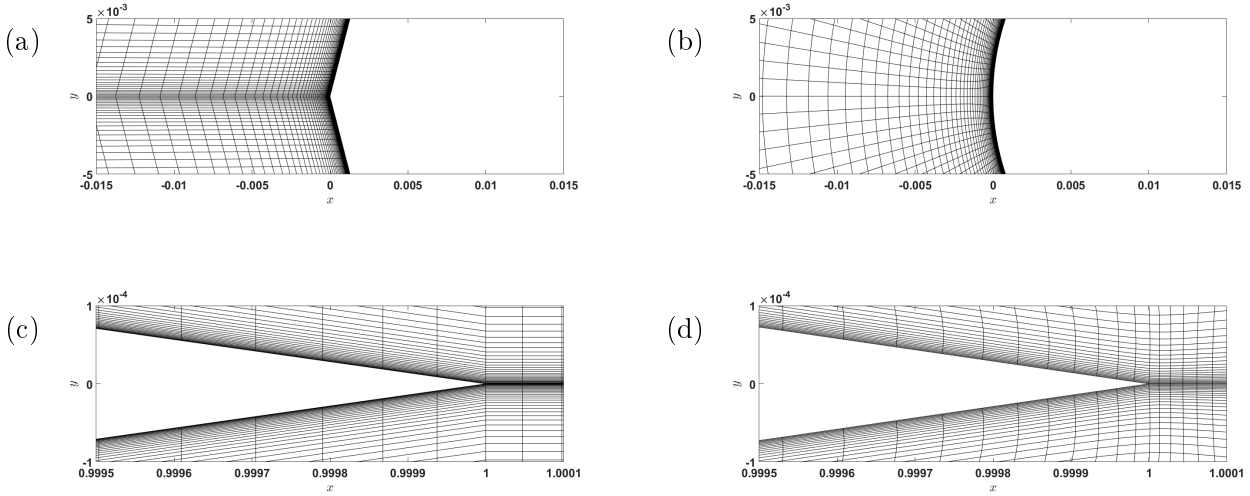

Figure 2.4: Grid comparison: (a) leading edge of the Fluent grid, (b) leading edge of the EWN-CGrid, (c) trailing edge of the Fluent grid, and (d) trailing edge of the EWN-CGrid.

	ANSYS Fluent structured grid	EWN-CGrid
Maximum skewness for $y^+ < 5$	0.78	0.38
Maximum aspect ratio for $y^+ < 5$	9×10^4	3×10^4
Average growth rate for $y^+ < 5$	i j 1.01 1.12	i j 1.01 1.14
Average growth rate	i j 26.0 1.12	i j 2.15 1.39

Table 2.1: ANSYS Fluent structured grid and EWN-CGrid properties: skewness, aspect ratio, and growth rate in the i and j varying index.

Chapter 3
VERIFICATION AND VALIDATION

In this section, we report the verification and validation results for the RANS modeling of the turbulent flow over airfoils as described in Ch. 2. First, through the verification study, we provide guidelines to setup such RANS computations. Then, through the validation by comparing the RANS results with published experiments for a turbulent flow over an airfoil [27], we provide information on the fidelity of RANS results. All our RANS computations were performed using ANSYS Fluent [17] using the SA-RC and SST-RC turbulence models and computational grids that were generated using our EWN-CGrid solver as described in Ch. 2.

3.1 Verification

For our verification test-cases, we aim to establishing the minimum computational domain size and grid resolution required to obtain converged results. These verification test-cases are performed using the NACA0012 airfoil at the Reynolds number based on the airfoil chord, Re_c, of 6×10^6. All the verification test-cases were run until the residuals of Reynolds averaged mass conservation Eq. (2.1), x and y momentum Eq. (2.2), and the turbulence model equations provided in output by ANSYS Fluent, are all smaller than 10^{-6}.

3.1.1 Computational domain size

In numerical simulations of fluid flows, the setting of the computational domain size is an important step for capturing the correct physics of the flow problem that we wish to model numerically while not wasting computational resources. In the present study, there is no boundary layer development before the flow reaches the airfoil, but the location of

inflow and outflow boundaries still affect the RANS flow solution due to the presence of the airfoil affecting the flow around it with respect to the far-field conditions. Thus, herein, we wish to assess the impact of different domain sizes to the RANS solution and provide our recommendation for what is the rationale for setting the domain size in our simulations.

The computational domain is shown in Fig. 2.1. L_u denotes the length of the radius of the semicircle with the origin at the airfoil trailing edge, and in the rectangular part of the grid, L_d denotes the length from the airfoil trailing edge to the outflow boundary. Tables. 3.1 and 3.2 show the test cases that we have performed to establish what is the minimum domain size to obtain converged results: ten cases of different upstream length, L_u, (i.e., different radii of the semicircle of the C-grid, Fig. 2.1), ten cases of different downstream lengths, L_d, from the trailing edge of the airfoil to the outlet.

Test-case	L_u	L_d
L_{u10}	10	25
L_{u20}	20	25
L_{u30}	30	25
L_{u40}	40	25
L_{u50}	50	25
L_{u60}	60	25
L_{u70}	70	25
L_{u80}	80	25
L_{u90}	90	25
L_{u100}	100	25

Table 3.1: Teat cases for computational domain size convergence with variation in the upstream length, L_u, and $L_d = 25$

Test-case	L_u	L_d
L_{d10}	50	10
L_{d20}	50	20
L_{d30}	50	30
L_{d40}	50	40
L_{d50}	50	50
L_{d60}	50	60
L_{d70}	50	70
L_{d80}	50	80
L_{d90}	50	90
L_{d100}	50	100

Table 3.2: Teat cases for computational domain size convergence with variation in the downstream length, L_d, and $L_u = 50$

The consideration of upstream length, L_u, consists of 10 cases as shown in Table 3.1, where L_u ranges from 10 to 100, while L_d is kept constant at 25. For all the verification cases, the inflow velocity is kept as uniform flow with zero degree angle of attack. The distribution of the pressure coefficient, C_p, and skin friction coefficient, C_f, along the horizontal line at $y = 0$, and the airfoil upper surface are examined and used as the convergence criterion for L_u and L_d. The convergence of the solutions is assessed qualitatively by plotting their profiles and, then, quantitatively by computing the relative change. The assessment of the convergence of computational domain size is used by computing the relative change in the numerical solution of C_p over successive domain sizes. Fig. 3.1a shows the distribution of C_p over the horizontal line from $x = -4$ to $x = 0$, and Fig. 3.1b shows the C_p distribution over the airfoil upper surface. Fig. 3.2a shows the C_p distribution over the airfoil upper surface, and Fig. 3.2b show the distribution of C_p over the horizontal line from $x = 1$ to $x = 11$. Fig. 3.1a, 3.1b, 3.2a, and 3.2b show that the C_p profiles converge as L_u and L_d values increase.

While the qualitative analysis gives insight into the influence of L_u and L_d on the numerical solution, a quantitative analysis is required to determine the final values of L_u and L_d best suited for the current study. We evaluate the convergence quantitatively by computing the relative change, $\epsilon_{2,1}$, in C_p between successive domain lengths:

$$\epsilon = \frac{C_{p,2} - C_{p,1}}{C_{p,1}}, \tag{3.1}$$

where $C_{p,1}$ and $C_{p,2}$ correspond to two successive domain lengths L_1 and L_2 for either L_u or L_d. The computation of the relative change for the upstream domain size cases is done by extracting values of C_p along the specified horizontal line for each upstream length case, and by computing ϵ using Eq. (3.1) for each case of subsequent increasing lengths. For example, the relative change, ϵ, between $L_u = 20$ and $L_u = 10$ is calculated using the C_p values along the horizontal line of the $L_u = 20$ and $L_u = 10$ cases. Table 3.3 shows the results of the relative change, ϵ, of pressure coefficient with respect to successive upstream domain lengths L_u. The relative change ϵ becomes smaller than 1% for the two domains with $L_u = 50$

and $L_u = 60$. Therefore, $L_u = 50$ is the recommended upstream domain length. The same method is applied to determine L_d. Table 3.4 shows the results of the relative change, ϵ, of C_p with respect to successive upstream domain sizes L_d. The relative change ϵ becomes smaller than 1% for the two domains with $L_d = 40$ and $L_d = 50$. Therefore, $L_d = 40$ is the recommended upstream domain length.

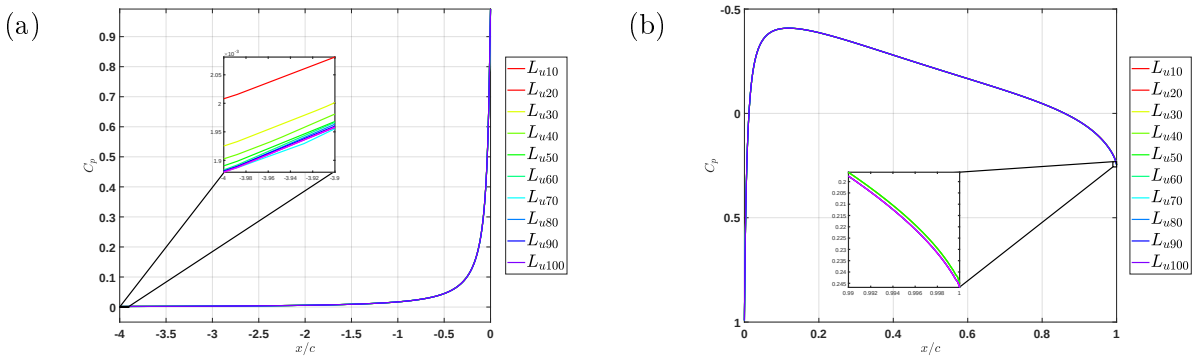

Figure 3.1: Effects of upstream computational domain size L_u: (a) C_p profile over horizontal line at $y = 0$, (b) C_p profile over a NACA0012 airfoil at $\alpha = 0°$ and $Re_c = 6 \times 10^6$.

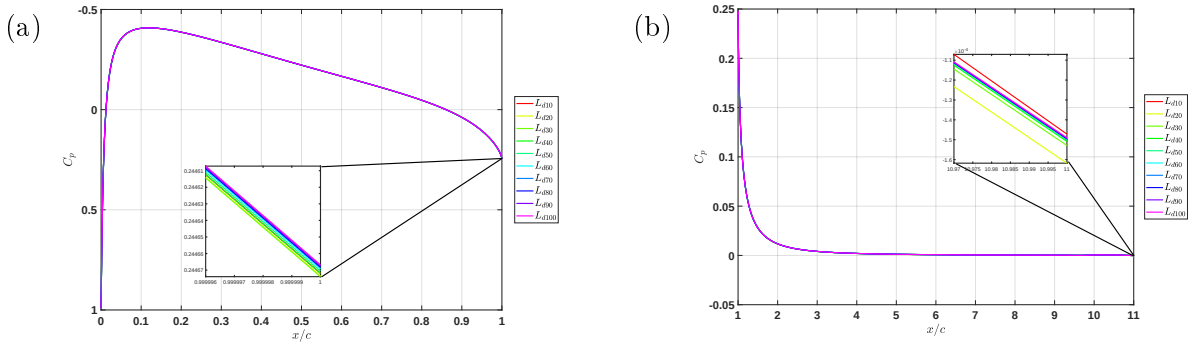

Figure 3.2: Effects of downstream computational domain size L_d: (a) C_p profile over airfoil, (b) C_p profile over horizontal line at $y = 0$

	$y = 0$ line, $x \in [-4, 0]$	Airfoil upper surface
$L_{u10,20}$	0.0413	0.0458
$L_{u20,30}$	0.0118	0.0128
$L_{u30,40}$	0.0074	0.0159
$L_{u40,50}$	0.0061	0.1951
$L_{u50,60}$	0.0070	0.0001
$L_{u60,70}$	0.0069	0.0046
$L_{u70,80}$	0.0048	0.0029
$L_{u80,90}$	0.0018	0.0012
$L_{u90,100}$	0.0025	0.0003

Table 3.3: Maximum relative change between successive solutions of C_p with the variation of the upstream domain length, L_u.

	$y = 0$ line, $x \in [1, 11]$	Airfoil upper surface
$L_{d10,20}$	0.6726	0.0094
$L_{d20,30}$	0.0995	0.0018
$L_{d30,40}$	0.0204	0.0008
$L_{d40,50}$	0.0065	0.0008
$L_{d50,60}$	0.0034	0.0008
$L_{d60,70}$	0.0021	0.0006
$L_{d70,80}$	0.0003	0.0001
$L_{d80,90}$	0.0017	0.0005
$L_{d90,100}$	0.0023	0.0005

Table 3.4: Maximum relative change between successive solutions of C_p with the variation of the downstream domain length, L_d.

3.1.2 Grid convergence

The grid convergence study is carried out using eight grids, case 1 to 4 where N_i is changed and N_j is fixed, and case 5 to 8 where N_i is fixed and N_j is varied as shown in Table. 3.5. The grid convergence study is carried out by computing the grid convergence index (GCI) using the procedure presented by Celik [6] for pressure coefficient, C_p, and the skin friction coefficient, C_f, over the airfoil's upper surface. The results of the GCI computations are listed in Table. 3.6. Based on the results of GCI between succesive grid resolutions of $O(10^{-2})$, for both the C_p and C_f solutions, we can consider the results for N_i converge with $N_i = 515$, and N_j converge with $N_j = 129$. Thus, the computational mesh with, 515×129 grid points is adopted for the validation in Ch. 3.2 and application runs in Ch. 4.

	N_i	N_j
Case 1	131	65
Case 2	259	65
Case 3	515	65
Case 4	1027	65
Case 5	515	33
Case 6	515	65
Case 7	515	129
Case 8	515	257

Table 3.5: Test cases of different grid resolutions for grid convergence

		C_p	C_f
N_i variation	$GCI_{3,2}$	2.74×10^{-1}	6.86×10^{-1}
	$GCI_{4,3}$	7.21×10^{-3}	4.53×10^{-2}
N_j variation	$GCI_{7,6}$	1.43×10^{-6}	1.73×10^{-2}
	$GCI_{8,7}$	2.32×10^{-4}	3.79×10^{-4}

Table 3.6: Grid convergence index(GCI) between successive solutions of different grid resolutions

3.2 Validation

3.2.1 Turbulence model comparison

To determine the RANS model to use in the current study among those available in Fluent, we have performed a comparison of the results of the one-equation Spalart-Allmaras (SA) model [23] and the two-equation shear-stress transport (SST) model [18], both with the curvature correction (RC) [21, 22] for the flow over a NACA0012 airfoil at $Re_c = 6 \times 10^6$ at $\alpha = 10^\circ$ and 15°. The RANS results were compared with the experiments of Ladson [15] and the numerical results of the CFL3D code by [7]. Table 3.7 shows C_D and C_L and the percentage errors computed with reference to the experimental measurements. Table 3.7 shows the comparison of C_D and C_L values between RANS, experiments and CFL3D results. Based on the better performance of the SA-RC model, i.e., closer C_D and C_L to the experimental measurements, we have adopted the SA-RC model than the SST-RC model for the formulation of the law in the application runs of Ch. 4.

		Ladson	CFL3D-SA	SA-RC	CFL3D-SST	SST-RC
C_D	$\alpha = 10^\circ$	0.01201	0.01179(1.8%)	0.01269(5.6%)	0.01236(2.9%)	0.01309(8.9%)
	$\alpha = 15^\circ$	0.01900	0.02066(8.7%)	0.02161(13.7%)	0.02219(16.7%)	0.02338(23%)
C_L	$\alpha = 10^\circ$	1.0707	1.0947(2.2%)	1.0718(0.1%)	1.0778(0.6%)	1.0587(1.1%)
	$\alpha = 15^\circ$	1.5129	1.5560(2.8%)	1.5283(1.0%)	1.5068(0.4%)	1.4780(2.3%)

Table 3.7: Turbulence model comparison with Ladson experimental results [15] of fixed transition

3.2.2 RANS comparison with experimental measurements

To validate the numerical solutions of the current study, we performed a comparison of the RANS results with the experimental measurements published by Wadcock [27] of a NACA4412 airfoil at the Reynolds number of $Re_c = 1.64 \times 10^6$ and with an angle of attack ranging from 0° to 14°. In accordance with the results from the computational domain size and grid convergence of Ch. 3.1, we used the domain size of $L_u = 50$, and $L_d = 40$ and the computational grid resolution of 515×129 grid points. The simulation parameters for the validation case are listed in Table 3.8.

Re_c	c (m)	L_u	L_d
1.64×10^6	1	50	40

Table 3.8: Flow parameters and domain size of the validation test-case

The inflow conditions, as described in Ch. 2.1.1, are maintained uniform, with the direction of the velocity vectors corresponding to the angle of attack α prescribed for each run. In the Wadcock [27] experiment, the flow over the airfoil was tripped at the leading edge and the RANS simulation has the turbulence conditions set at the domain inflow. Fig. 3.3 shows the distribution of the pressure coefficient, C_p, over the airfoil for a series of angle of attacks, 0° to 14°, that is also reported in the Wadcock [27] experiments. The C_p distribution of the RANS simulation over the airfoil matches the experimental measurements for lower angles of attack and the results start to deviate as the airfoil approaches maximum lift conditions, i.e., for $\alpha \geq 12°$. For a quantitative comparison, we calculate the L_2 norm, σ, between the C_p obtained from the RANS results with Wadcock [27] experimental data. Table 3.9 shows that at the incipient separation angle, $\alpha = 1.015°$, σ is about 0.04, and, as the angle of the NACA4412 airfoil increases, the σ also increases. Eventually, at $\alpha = 14°$, σ becomes 0.3883.

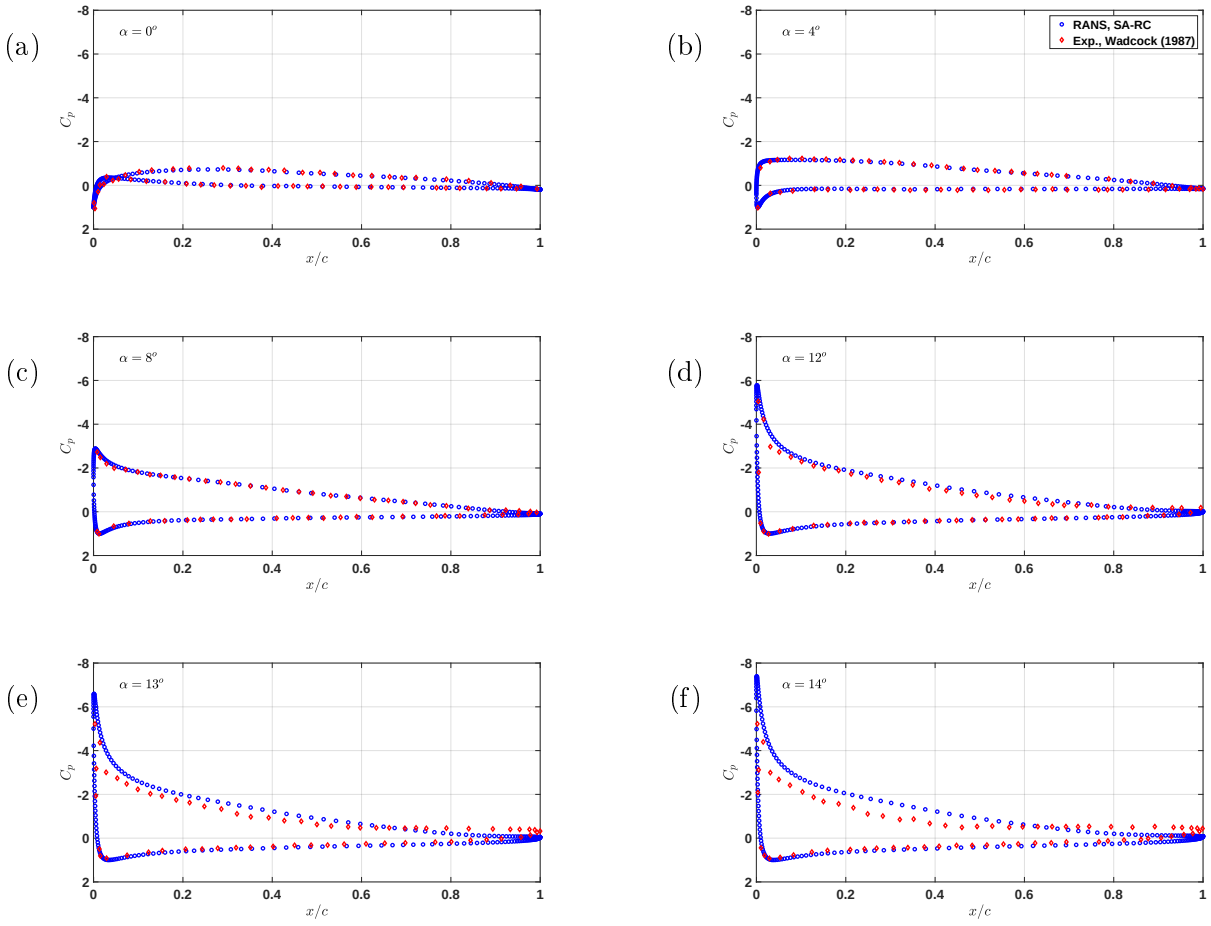

Figure 3.3: C_p comparison of RANS SA-RC results (blue circles) with Wadcock [27] experimental data (red diamonds) for the turbulent flow over a NACA4412 airfoil at: (a) $\alpha = 0°$, (b) $\alpha = 4°$, (c) $\alpha = 8°$, (d) $\alpha = 12°$, (e) $\alpha = 13°$, and (f) $\alpha = 14°$.

α	0°	4°	8°	12°	13°	14°
σ	0.0477	0.0345	0.0416	0.1342	0.2691	0.3883

Table 3.9: L_2 norm of C_p comparison of RANS SA-RC results with Wadcock [27] experimental data for different angles of attack, $\alpha = 0°$ to 14°.

The comparison of the velocity profiles at $\alpha = 12^\circ$ in the boundary layer over the airfoil are shown in Fig. 3.4. From the velocity profiles at $x/c = 0.529$ (Fig. 3.4a), where the flow is still attached, the tangential velocity and the normal velocity of the RANS results match the experimental measurements. The velocity overshoot at the edge of the boundary layer is also effectively captured by the RANS results with a percentage error of 3.95%. At $x/c = 0.815$, the velocity profiles show the effects of the adverse pressure gradient where the maximum tangential velocity is of a smaller value than at $x/c = 0.529$, the experimental measurements also indicate that the flow is still attached to the airfoil. For the velocity profile at $x/c = 0.952$, the reversed flow can be clearly seen in the tangential velocity profile for both the RANS and experimental data, with the experimental results having a higher reverse flow velocity. While the RANS results for $x/c = 0.815$ and 0.952 deviates more from the experimental results, the prediction of the RANS that the flow separates is consistent with the experimental results.

It should be noted that although the RANS results deviate from the experimental measurements in the presence of large flow separations at higher angles of attack, the incipient separation over the NACA4412 airfoil occurs at $\alpha \simeq 1^\circ$ for which the RANS prediction of C_p is matching the experimental data of Wadcock at both $\alpha = 0^\circ$ and 4°. Thus, since the RANS predictions are accurate at small angles of attack for attached or mildly separated flows, but only fail at large angles of attack as the airfoil approaches its maximum lift, then, this result gives us enough confidence in the fidelity of the RANS results for using this modeling methodology to investigate the existence of a law of incipient separation for airfoils.

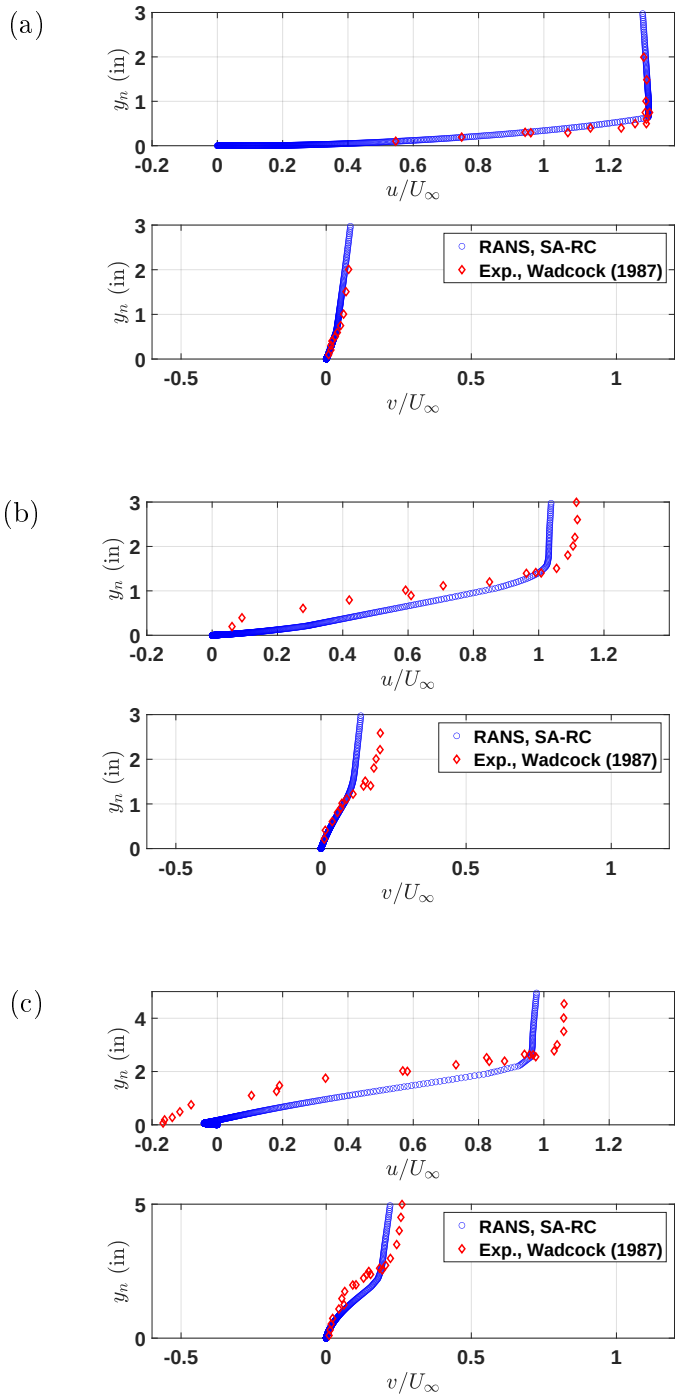

Figure 3.4: Velocity components tangential and vertical to the airfoil comparison of RANS SA-RC with Wadcock [27] experimental data, where y_n represents the normal distance from the airfoil upper surface at three different locations: (a) $x/c = 0.529$, (b) $x/c = 0.815$, and (c) $x/c = 0.952$.

Chapter 4

THE LAW OF INCIPIENT SEPARATION OVER AIRFOILS

We investigate the phenomenon of flow separation over twenty-nine airfoils, and study the effects of the airfoil geometry and upstream flow parameters. We search for a potential criterion for the incidence of incipient turbulent flow separation over the airfoil with the goal to find key geometrical features which are related to the separation of turbulent flows over airfoils. Recently, Lu, Aithal & Ferrante [16] determined that the maximum slope and the height-to-length ratio of a ramp are the key geometrical parameters for determining the incipience of turbulent flow separation. Along the same lines, herein, we define a new geometric parameter for an airfoil that we call the "characteristic line" of the airfoil. The characteristic line is the line joining the point P, viz., the location of maximum y value of the airfoil profile, and the airfoil trailing edge (T.E.). The characteristic line is represented by the blue line in Fig. 4.1, which shows the geometric characteristics of the NACA4412 airfoil at two angles of attack. For convenience, we define as characteristic slope, m_{P}, the absolute value of the slope of the characteristic line. The comparison of the two characteristic lines in Fig. 4.1 for $\alpha = 0^{\circ}$ and 10° shows that as the angle of attack increases, the characteristic slope increases as well. This will allow us to replace the dependence on angle of attack with the characteristic slope in the formulation of the law below.

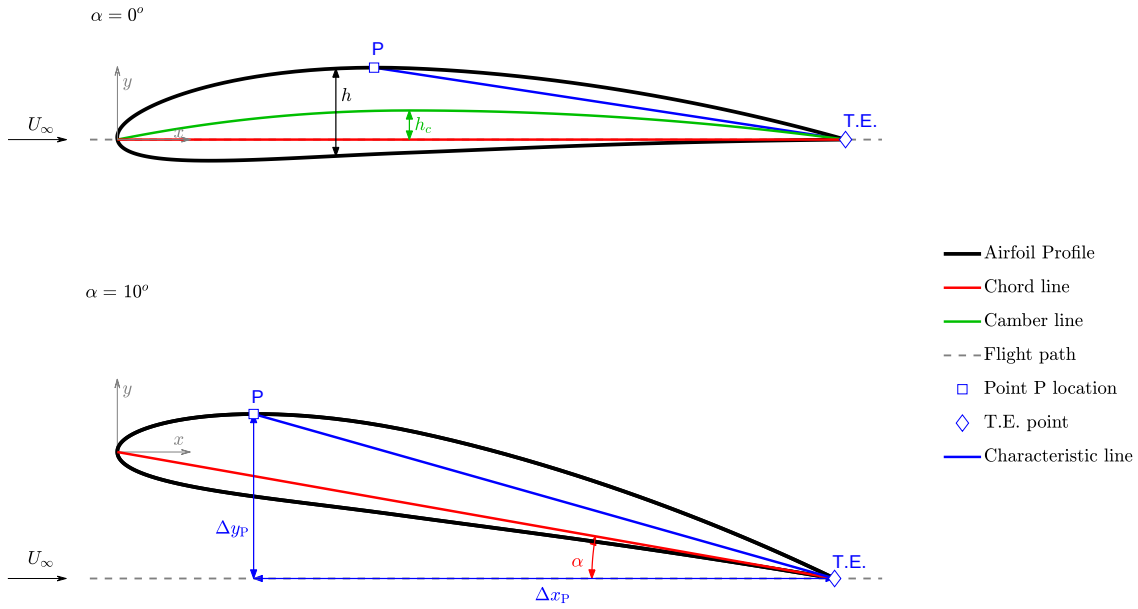

Figure 4.1: Airfoil's geometric characteristics at $\alpha = 0°$ and $\alpha = 10°$. The colored lines in the plot represents the main characteristics lines of the airfoil, the square symbol represents P, i.e.,the point of maximum y value on the airfoil profile, the diamond symbol represents the trailing edge (T.E.) of the airfoil, and Δx_P and Δy_P are the streamwise and vertical distance of P from the T.E..

4.1 Computation of critical angle of attack

For five NACA airfoils among those studied, Fig. 4.2a shows the profiles of the minimum skin friction coefficient, $C_{f_{\min}}$, as a function of the angle of attack, and Fig. 4.2b shows the profiles of $C_{f_{\min}}$, as a function of the characteristic slope, m_P. For a given airfoil, the increase in the angle of attack results in a higher characteristic slope (Fig. 4.1) and, thus, a higher adverse pressure gradient which, in turn, reduces the minimum skin-friction coefficient, $C_{f_{\min}}$, and

eventually leads to flow separation ($C_{f_{\min}} < 0$). Therefore, there exists a critical angle of attack, denoted as α_{crit}, for which the flow has an incipient separation point on the airfoil upper surface, i.e., where $C_{f_{\min}} = 0$. We denote the subscript "crit" for "critical" for the case where incipient separation occurs. At the same α or m_{P}, different airfoils may experience different $C_{f_{\min}}$. For example, as shown in Fig. 4.2a, the NACA0015 airfoil has a critical angle of attack $\alpha_{\text{crit}} = 2.48°$, while at the same angle of attack, the NACA0018 experiences flow separation ($C_{f_{\min}} < 0$), and the flow over the NACA0012 remains attached ($C_{f_{\min}} > 0$). Fig. 4.3a shows, for the NACA0015 airfoil, the way we determined α_{crit} by using a sixth-order polynomial curve fitting to the RANS results. For the case of the NACA0015 airfoil at $Re_c = 1.64 \times 10^6$, the intersection of the fitted line and $C_{f_{\min}} = 0$ is denoted by the blue circle, and α_{crit} is represented by the red asterisk in Fig. 4.3b. The critical characteristic slope, $m_{\text{P}_{\text{crit}}}$, is the characteristic slope at the critical angle of attack, α_{crit}.

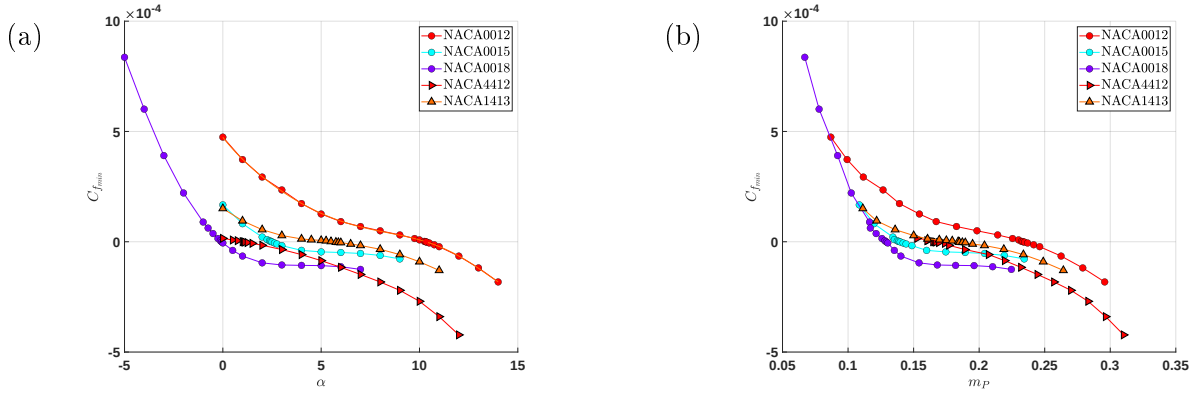

Figure 4.2: Minimum skin friction coefficient, C_f, as a function of (a) airfoil angle of attack, α, (b) airfoil characteristic slope, m_{P}.

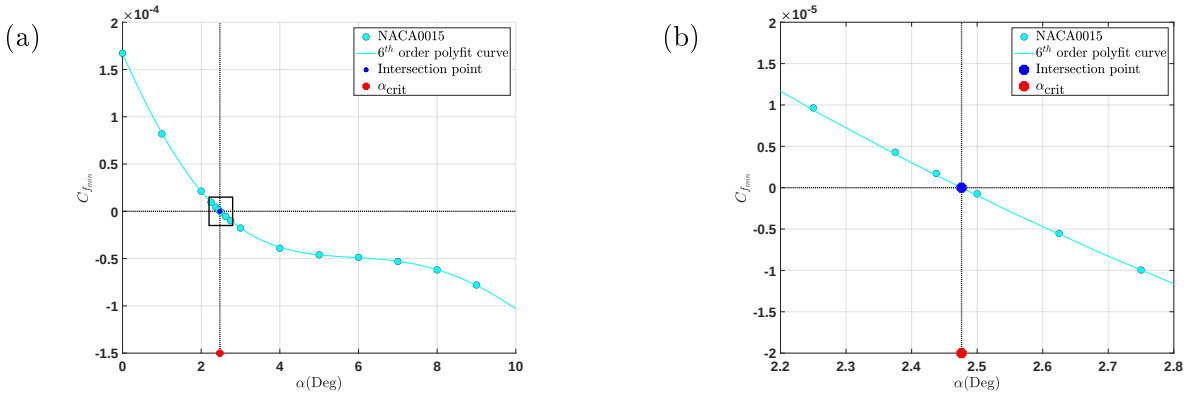

Figure 4.3: Determination of the α_{crit} (red symbol) by finding the intersection (blue symbol) of the RANS data fitted sixth-order polynomial, and the $C_{f_{\text{min}}} = 0$ line. (a) $C_{f_{\text{min}}}$ as a function of α, (b) $C_{f_{\text{min}}}$ as a function of α (area shown in black box of (a)).

4.2 Effects of airfoil angle of attack C_p and C_f

Fig. 4.4a shows the profile of the NACA4412 airfoil's upper surface at different angles of attack. Fig. 4.4b and 4.4c show the effect of angle of attack on the C_p and C_f profiles for the same airfoil. As the angle of attack increases, the characteristic slope (4.4a) increases, and the flow over the upper surface of the airfoil experiences a larger magnitude of C_p, and, thus, a larger adverse pressure gradient (4.4b), which, in turn, reduces the $C_{f_{\text{min}}}$ in the rear end of the airfoil. The green lines in Fig. 4.4 denote cases for which the flow remain attached to the airfoil surface ($C_{f_{\text{min}}} > 0$), the red lines denote the airfoil profiles which experiences flow separation ($C_{f_{\text{min}}} < 0$), and the black lines represent the case of incipient separation, $C_{f_{\text{min}}} = 0$, i.e., the airfoils are at the critical angle of attack, α_{crit}. A zoomed in region of the airfoil trailing edge (blue box) is also shown in Figs. 4.4b and 4.4c. The pressure distribution over the separated region gets flatter in accordance to what was described in [27].

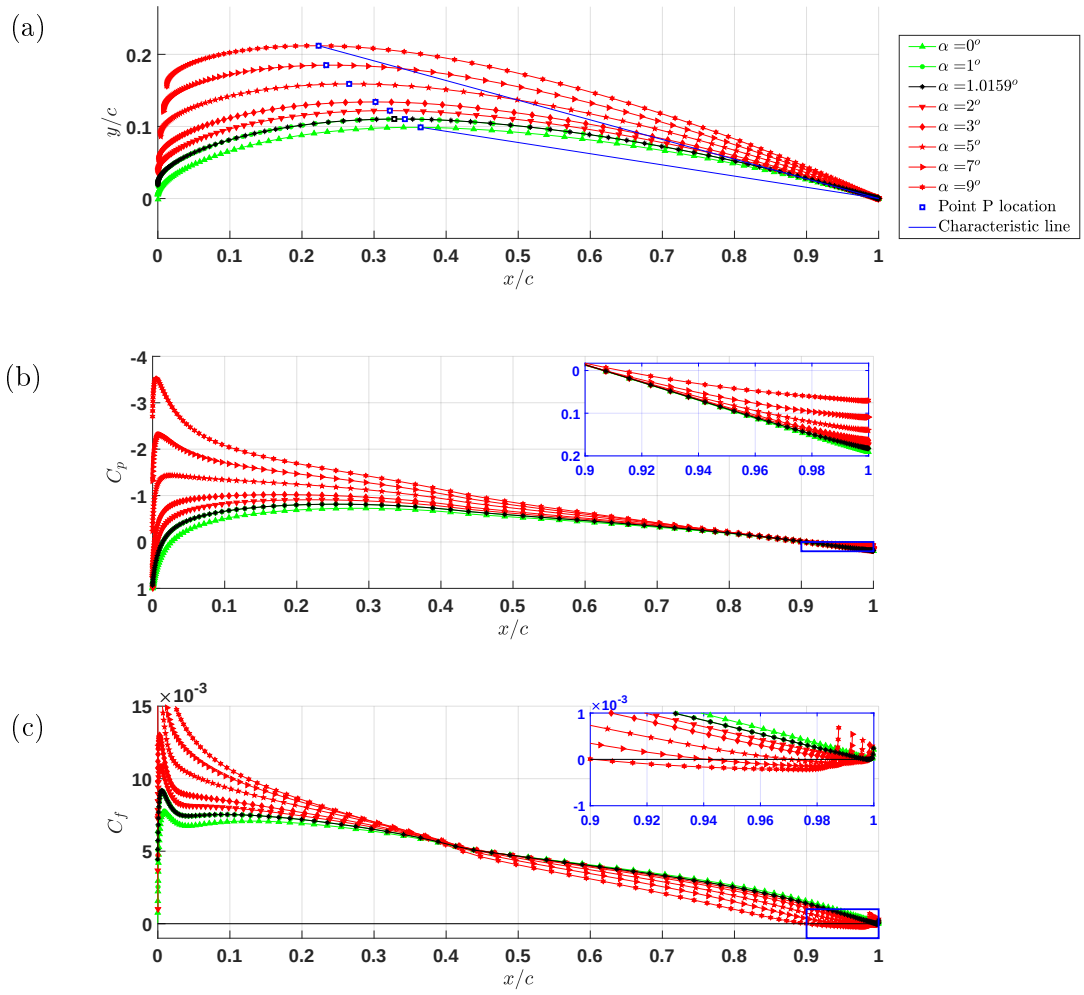

Figure 4.4: Effects of airfoil angle of attack over C_p and C_f for the NACA4412 airfoil at $Re_c = 1.64 \times 10^6$ (a) NACA4412 airfoil for different angles of attack, α, (b) C_p distribution over the upper surface of the airfoil for different α, and (c) C_f distribution over the upper surface of the airfoil for different α. Green lines: attached flow ($C_{f_{\min}} > 0$); black line: incipient separation ($C_{f_{\min}} = 0$); red lines: separated flow ($C_{f_{\min}} < 0$).

4.3 Effects of geometry on C_p and C_f

4.3.1 Airfoil thickness

All the airfoil profiles investigated in the current study are NACA four or six-digits airfoils. Thus, they are smooth airfoils, i.e., the profile and their first derivative is continuous, but the second derivative may have a discontinuity. In this section, we study the effect of airfoil thickness on flow separation. Fig. 4.5a shows the airfoil's upper profiles at $\alpha = 0°$, i.e., symmetric airfoils for which the thickness as percentage of the chord is expressed by the last two digits of the NACA airfoils that were varied from 12 to 21. All the airfoils shown in Fig. 4.5a share the same x-location of maximum thickness at $x/c = 0.3$.

Fig. 4.5b and 4.5c show the C_p and C_f profiles for the NACA airfoils of Fig. 4.5a at $\alpha = 0°$ and $Re_c = 1.64 \times 10^6$. As the thickness increases, the characteristic slope increases (4.5a), and the flow over the upper surface of the airfoil experiences a larger magnitude of C_p, and, thus, a larger adverse pressure gradient (4.5b), which, in turn, reduces the $C_{f_{\min}}$ in the rear end of the airfoil (4.5c).

4.3.2 Airfoil camber

Fig. 4.6 shows the effects of the airfoil camber on the distribution of C_p and C_f over the airfoil upper surface. In Fig. 4.6a shows the NACA airfoils with the same thickness of 13%, an increasing camber from 0 to 4% of the chord which is located at 40% of the chord at $\alpha = 0°$. Fig. 4.6b and 4.6c show the C_p and C_f profiles of the airfoils at of Fig. 4.6a at $\alpha = 0°$ and $Re_c = 1.64 \times 10^6$. As the camber increases, the characteristic slope increases (4.6a), and the flow over the upper surface of the airfoil experiences a larger magnitude of C_p, and, thus, a larger adverse pressure gradient (4.6b), which, in turn, reduces the $C_{f_{\min}}$ in the rear end of the airfoil (4.6c).

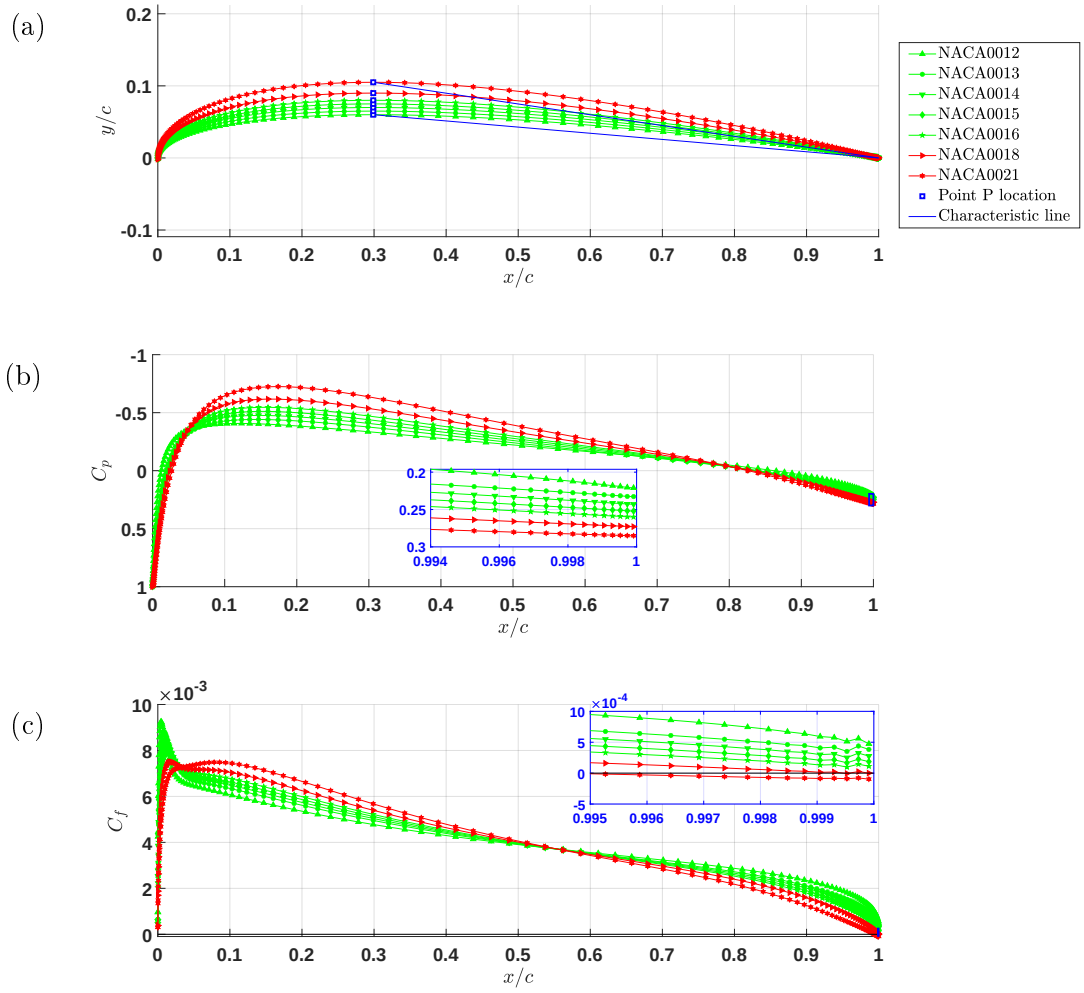

Figure 4.5: Effects of airfoil thickness over C_p and C_f for NACA four-digits symmetric airfoils at $\alpha = 0°$ and $Re_c = 1.64 \times 10^6$ (a) NACA four-digits symmetric airfoils for different thickness, h, (b) C_p distribution over the upper surface of the airfoil for different thickness, h, and (c) C_f distribution over the upper surface of the airfoil for different thickness, h. Green lines: attached flow ($C_{f_{\min}} > 0$); red line: separated flow ($C_{f_{\min}} < 0$).

From the result of Figs. 4.4, 4.5, and 4.6, we conclude that the airfoil characteristic slope, m_{P}, along with the airfoil thickness, h, and airfoil camber, h_c, are key geometrical features in the separation of the turbulent flow over airfoils. In Ch. 4, we will investigate and show

if by using these key parameters it is possible to determine a scaling law for predicting the incipiency of turbulent flow separation over smooth airfoils.

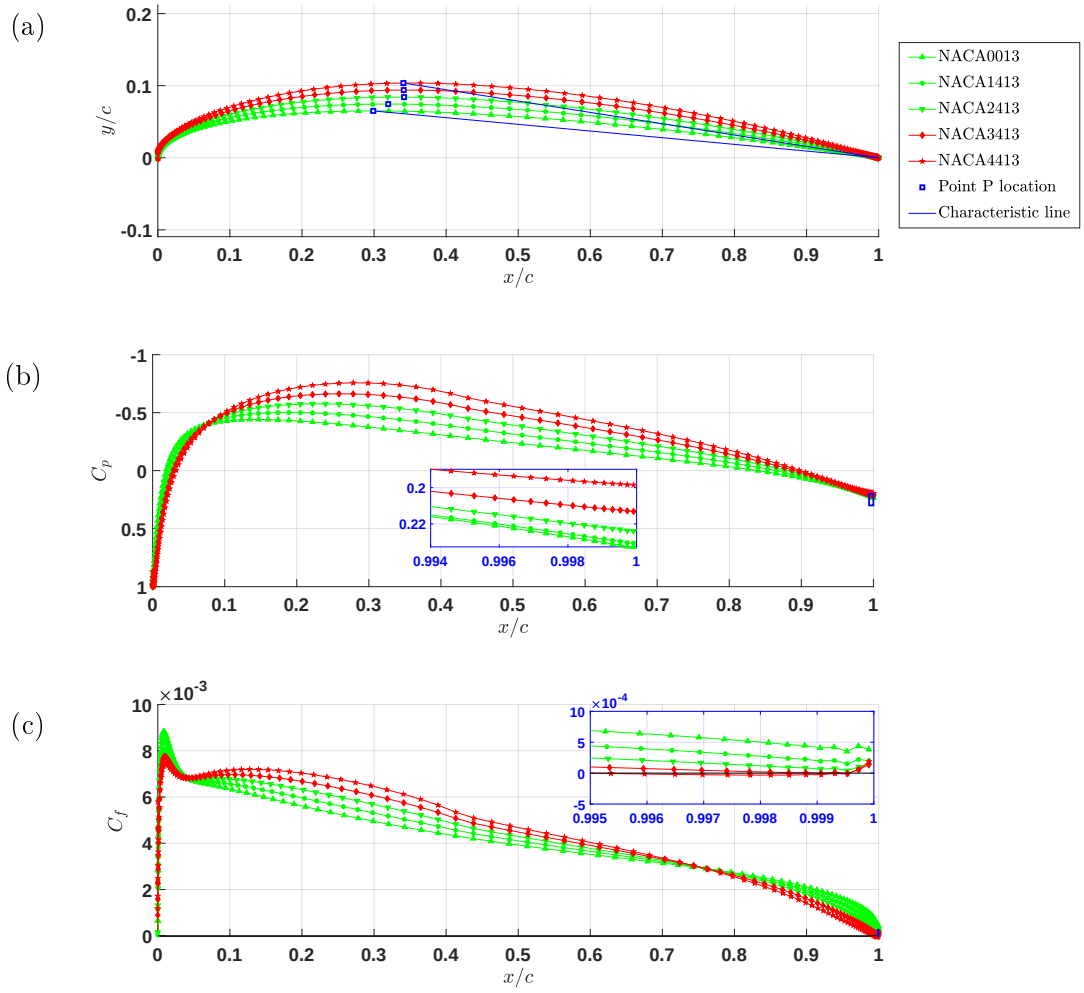

Figure 4.6: Effects of airfoil camber over C_p and C_f for NACA0013 to NACA4413 airfoils at $\alpha = 0°$ and $Re_c = 1.64 \times 10^6$ (a) NACA airfoils for different camber, h_c, (b) C_p distribution over the upper surface of the airfoil for different camber, h_c, and (c) C_f distribution over the upper surface of the airfoil for different camber, h_c. Green lines: attached flow ($C_{f_{\min}} > 0$); red line: separated flow ($C_{f_{\min}} < 0$).

4.4 *Effects of flow parameters on* C_f

4.4.1 Effect of Reynolds number

To investigate the sensitivity of the RANS results to Reynolds numbers, test-cases at three different Reynolds numbers ($Re_c = 1.64 \times 10^6$, $Re_c = 3.28 \times 10^6$ and $Re_c = 6 \times 10^6$) were studied. Fig. 4.7 shows the effect of the Reynolds number on C_p and C_f profiles over the NACA4412 airfoil at an angle of attack of 4°. As Re_c is increased, the turbulent flow has higher momentum near the airfoil's surface under a nearly identical adverse pressure gradient (Fig. 4.7a) which is mostly determined by the shape of the airfoil and the angle of attack, resulting in increasing the $C_{f_{\min}}$ and delaying the $C_{f_{\min}}$ location towards the T.E. of the airfoil as shown in Fig. 4.7b.

Thus, this concludes that a higher Re_c leads to a higher critical angle of attack, α_{crit}, for a given airfoil, and a higher critical characteristic slope, $m_{\text{P}_{\text{crit}}}$.

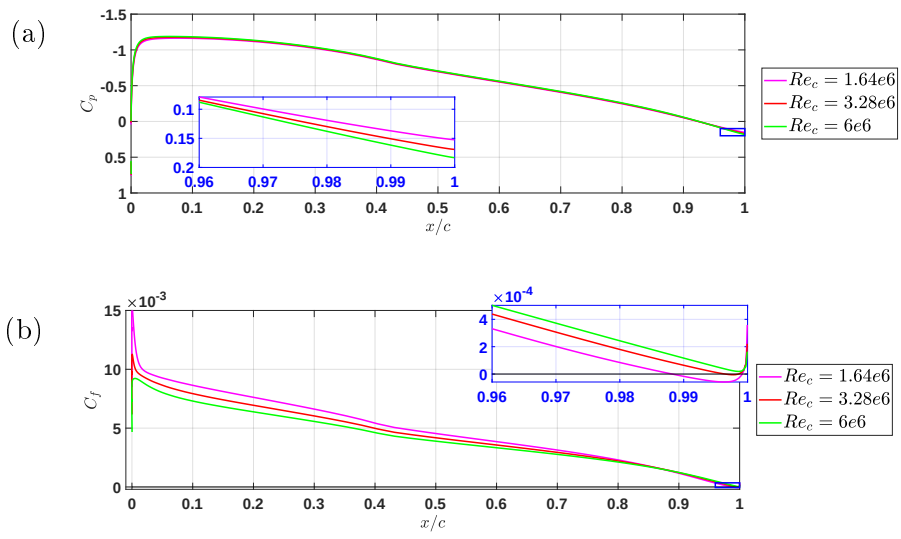

Figure 4.7: Effects of Reynolds number on C_p and C_f on the NACA4412 airfoil at angle of attack = 4°. (a) C_p distribution over the upper surface of the airfoil for different Re_c, and (b) C_f distribution over the upper surface of the airfoil for different Re_c.

4.5 The law of incipient separation

4.5.1 Formulation of the law of incipient separation for $Re_c = 1.64 \times 10^6$

From sections 4.2 and 4.3, we have seen that along the airfoil upper surface, after a brief expansion, the flow experiences an adverse pressure gradient (as shown by the C_p profiles) that reduces the skin-friction coefficient and may lead to flow separation ($C_{f_{\min}} < 0$). Such profiles of C_p and C_f are affected by the angle of attack, α, the characteristic slope, m_{P}, the airfoil thickness, h, and the airfoil camber, h_c. To find a relationship between flow separation and the geometrical parameters mentioned above, we have considered 29 of the 32 airfoils shown in the legend of Fig. 4.8c, i.e., all of them with the exception of NACA1412, NACA2213, and NACA2312 airfoils, which were used, instead, after deriving the law to verify that they also produce results that fall within the law.

In the following analysis, we have examined the geometrical properties and the RANS results at $Re_c = 1.64 \times 10^6$ at the critical angle of attack, α_{crit}, for which, $C_{f_{\min}} = 0$. For each airfoil, α_{crit} was determined following the procedure described in Ch. 4.2 and graphically explained via Fig. 4.3. We define two parameters, $\hat{m}_{\mathrm{P}}$ and $\hat{\Gamma}$, which combine the characteristic slope, m_{P}, and airfoil geometrical features of the P point at zero angle of attack, denoted by α_0, as

$$\hat{m}_{\mathrm{P}} = m_{\mathrm{P}} \left(\frac{x_{\mathrm{P}_{\alpha_0}}}{m_{\mathrm{P}_{\alpha_0}} y_{\mathrm{P}_{\alpha_0}}} \right)^{0.5}, \tag{4.1}$$

$$\hat{\Gamma} = \left(m_{\mathrm{P}_{\alpha_0}} y_{\mathrm{P}_{\alpha_0}} x_{\mathrm{P}_{\alpha_0}} \right)^{0.5}, \tag{4.2}$$

where $x_{\mathrm{P}_{\alpha 0}}$ and $y_{\mathrm{P}_{\alpha 0}}$ are the x/c and y/c values, respectively, of point P at $\alpha = 0°$ (Fig. 4.1), and $m_{\mathrm{P}_{\alpha 0}}$ is the characteristic slope at $\alpha = 0°$. Fig. 4.8a shows the $\hat{\Gamma}$ as a function of $\hat{m}_{\mathrm{P}_{\mathrm{crit}}}$. The data in Fig. 4.8a are scattered, however, as we modify Eq. (4.2) to obtain $\tilde{\Gamma}$ by introducing airfoil thickness, h, to the definition of $\hat{\Gamma}$ as

$$\tilde{\Gamma} = \left(m_{\mathrm{P}_{\alpha_0}} y_{\mathrm{P}_{\alpha_0}} x_{\mathrm{P}_{\alpha_0}} \right)^{0.5} h + \frac{h}{10}, \tag{4.3}$$

the data are grouped by the airfoil thickness as shown in Fig. 4.8b, corresponding to Eq. (4.3). Next, we introduce airfoil thickness, h, and camber, h_c, to the definition of $\hat{m}_{\mathrm{P}}$ to obtain $\tilde{m}_{\mathrm{P}}$ as

$$\tilde{m}_{\mathrm{P}} = m_{\mathrm{P}} \left(\frac{x_{\mathrm{P}_{\alpha_0}}}{m_{\mathrm{P}_{\alpha_0}} y_{\mathrm{P}_{\alpha_0}}} \right)^{0.5} - \left[10 \left(\frac{1}{h} - \frac{1}{100} \right) + 1 \right] h_c h - \frac{h^2}{100} - \frac{h}{5}, \tag{4.4}$$

so that the data collapse closer to a second-order polynomial as shown in Fig. 4.8c. We obtain a second order polynomial fit for all twenty-nine critical airfoils, thereby indicating the law of incipient separation over airfoils at $Re_c = 1.64 \times 10^6$ as:

$$\tilde{\Gamma} = a\tilde{m}_{\mathrm{P}}^2 + b\tilde{m}_{\mathrm{P}} + c, \tag{4.5}$$

where $a = 0.0209$, $b = -0.1194$, and $c = 1.3274$.

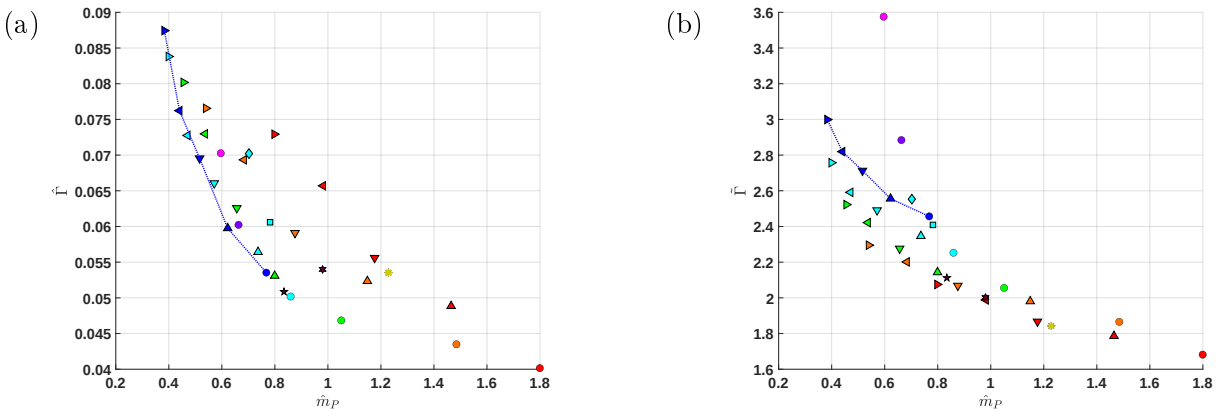

(c)

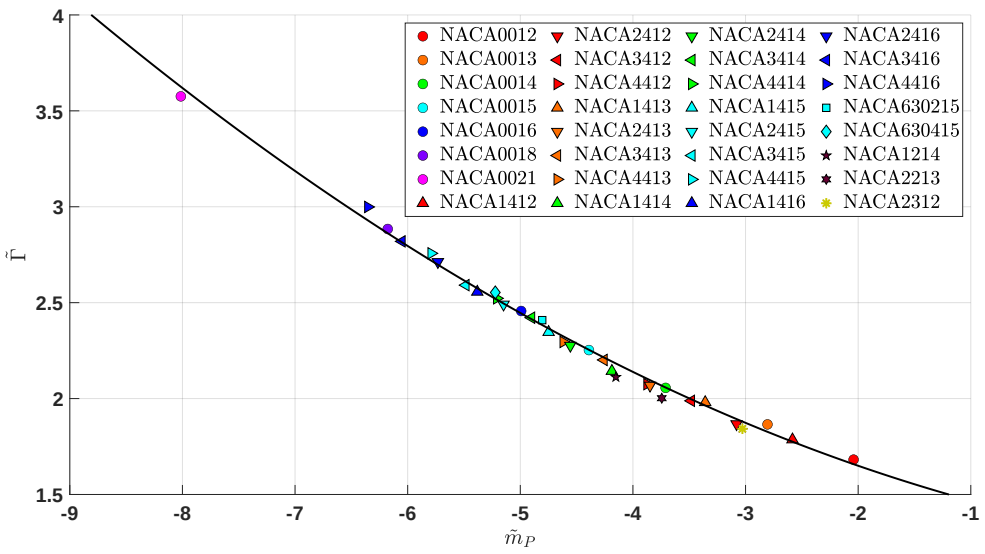

Figure 4.8: Law formulation steps of data modification to achieve data collapse: (a) $\hat{m}_{\mathrm{P}}$ vs $\hat{\Gamma}_{\mathrm{P}}$, (b) $\hat{m}_{\mathrm{P}}$ vs $\hat{\hat{\Gamma}}_{\mathrm{P}}$, (c) $\hat{m}_{\mathrm{P}}$ vs $\tilde{\Gamma}_{\mathrm{P}}$, (d) $\hat{\hat{m}}_{\mathrm{P}}$ vs $\tilde{\Gamma}_{\mathrm{P}}$, (e) $\tilde{m}_{\mathrm{P}}$ vs $\tilde{\Gamma}_{\mathrm{P}}$. The symbols used for each airfoil where chosen such that the same color represents airfoils of the same thickness, and the same symbol represents airfoils of the same maximum camber.

Next, we plot the $\tilde{\Gamma}$ versus $\tilde{m}_{\mathrm{P}}$ for all the airfoils and angles of attack studied at $Re_c = 1.64 \times 10^6$. In Fig. 4.9, the critical conditions ($C_{f_{\min}} = 0$) are represented by the colored symbols where the different colors correspond to different airfoil's cambers and thicknesses, while empty circles denote that the flow stays attached ($C_{f_{\min}} > 0$), and filled black circles indicate that the flow is separated ($C_{f_{\min}} < 0$). The gray area located in the upper right region in Fig. 4.9 shows the region where the RANS results become unreliable based on our validation test-case of Ch. 3. As we recall from Fig. 3.3, the RANS results match with the experimental measurements until the airfoil approaches its maximum lift conditions. For the NACA4412 airfoil, the experiments show that such conditions occur at angles of attack exceeding 12°. For the present study, airfoil incipient separation occurs well within the region that RANS simulation is reliable. In Fig. 4.9, we observe that the flow separates ($C_{f_{\min}} < 0$) over those airfoil which lie on the right-hand side of the solid line representing the law, while

it stays attached ($C_{f_{\min}} > 0$) over those airfoils that lie on the left of the law. Therefore, given an airfoil geometry, which fixes the $\tilde{\Gamma}$, we can determine whether the flow separates by using the following criterion:

$$\begin{cases} \tilde{m}_{\mathrm{P}} > \tilde{m}_{\mathrm{P}_{\mathrm{crit}}} \ \rightarrow \ \text{Separated flow} \ , \\ \tilde{m}_{\mathrm{P}} < \tilde{m}_{\mathrm{P}_{\mathrm{crit}}} \ \rightarrow \ \text{Attached flow.} \end{cases} \tag{4.6}$$

The standard deviation (L_2 norm), σ, is used to evaluate data scatter from the law. The L_2 norm is calculated based on the deviation of $\tilde{m}_{\mathrm{P}}$ at the critical value as derived from the simulation results, and the $\tilde{m}_{\mathrm{P}}$ value derived from the best fit 2^{nd} order polynomial fit of Eq. (4.5). The two dotted lines in Fig. 4.9 show a bandwidth of $2\sigma = 0.1726$ around the polynomial fit. The normalized standard deviation, $\bar{\sigma}$, is computed by dividing the L_2 norm with the mean of $|\tilde{m}_{\mathrm{P}}|$ for all the airfoils in Fig. 4.9 except the last three airfoils in the legend of Fig. 4.8c: NACA1214, NACA2213, and NACA2312. The normalized standard deviation of the data shown in Fig. 4.9 is $\bar{\sigma} = 0.0186$, i.e., the data normalized standard deviation from the polynomial fit (Eq. (4.5)) is smaller than 2%.

The RANS results obtained over the three airfoils, NACA1214, NACA2213, and NACA2312, at $Re_c = 1.64 \times 10^6$ were used to verify the derived law. The three airfoils vary in thickness, camber value and camber location and were not used to formulate the law. Fig. 4.9 shows that all three airfoils are close to the law of incipient separation, Eq. (4.5), and satisfy Eq. (4.6).

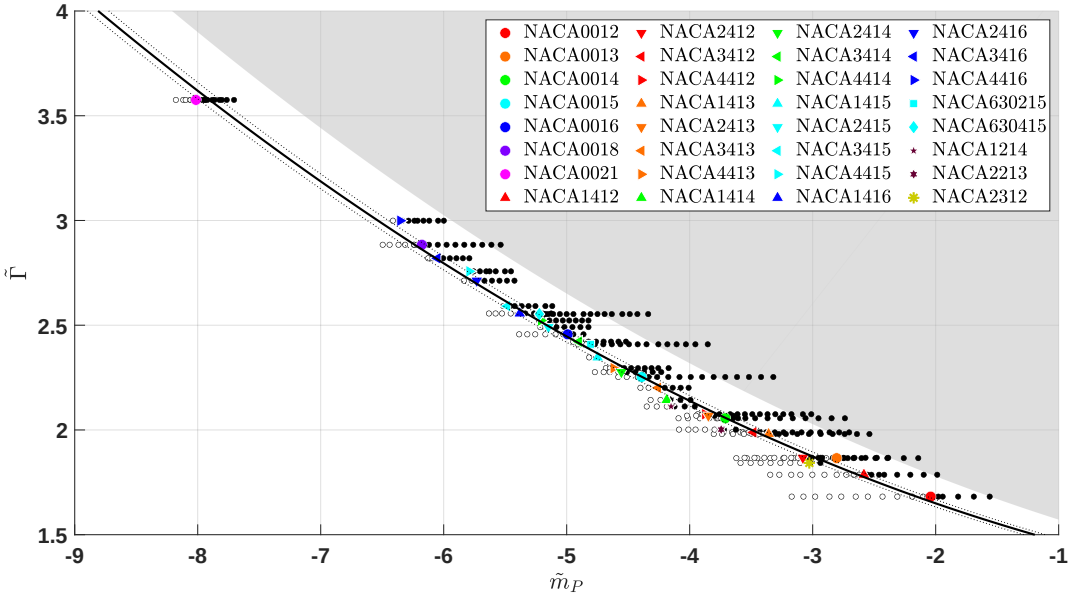

Figure 4.9: Data distribution of $\tilde{\Gamma}$ versus $\tilde{m}_{\mathrm{P}}$ for all the RANS simulations performed at $Re_c = 1.64 \times 10^6$ for different angles of attack. The data from the same airfoil lie on a horizontal line since $\tilde{\Gamma}$ is constant for a given airfoil. The colored symbols denote incipient separation ($C_{f_{\min}} = 0$), empty circles denote attached flow ($C_{f_{\min}} < 0$), and black circles denote separated flow ($C_{f_{\min}} > 0$). The solid black line is the data polynomial fit given by Eq. (4.5), and the dotted lines represent delineate a bandwidth of 2σ . The gray area indicates the RANS uncertainty region, i.e., the region in which the RANS prediction of $C_{f_{\min}}$ fails because of large separation.

4.5.2 Reynolds number effects on the law of incipient separation

Next, we investigate the effects of the Reynolds number on the law of incipient separation, Eq. (4.5). Fig. 4.10a shows the critical values of $\hat{\Gamma}$ (Eq. (4.2)) plotted as a function of $\hat{m}_{\mathrm{P}}$ (Eq. (4.1)) for the airfoils: NACA1412 to NACA4412, NACA1416 to NACA4416, and NACA0021 for $Re_c = 1.64 \times 10^6$, 3.28×10^6, and 6×10^6. It is seen in Fig. 4.10a that as the Reynolds number increases, the critical $\hat{m}_{\mathrm{P}}$ shifts to the right on the horizontal axis for

NACA1412 to NACA4412. Similarly to Ch. 4.5.1, we plot $\tilde{\Gamma}$ (Eq. (4.3)) as a function of $\tilde{m}_{\mathrm{P}}$ (Eq. (4.4)) in Fig. 4.10b such that the data collapse closer to three different second-order polynomials corresponding to $Re_c = 1.64 \times 10^6$, 3.28×10^6, and 6×10^6. Therefore, we obtain the following second-order polynomial fit for critical airfoils, whose coefficients scale the data based on the Reynolds number Re_c which demonstrates that the data distribution can be fitted by different second-order polynomials for different Reynolds numbers. The three unique Reynolds numbers generate three unique sets of constants for the second-order polynomial. As a result, we modify each constant with a Reynolds number dependency to generate unique polynomials for different Reynolds numbers. Finally, the law of incipient separation for $Re_c \in [1.64 \times 10^6, 6 \times 10^6]$ is given as,

$$\tilde{\Gamma} = \left(\beta_1 Re_c^{-\gamma}\right) \tilde{m}_{\mathrm{P}}^2 + \left(\beta_2 Re_c^{\gamma}\right) \tilde{m}_{\mathrm{P}} + \beta_3 Re_c^{-\gamma/10}, \tag{4.7}$$

where $\beta_1 = 0.64284$, $\beta_2 = -0.0038787$, $\beta_3 = 1.8699$, and $\gamma = 0.23944$.

The standard deviations of the data distribution in Fig. 4.11 are: $\sigma = 0.09$ for $Re_c = 1.64 \times 10^6$ (Fig. 4.11a); $\sigma = 0.1144$ for $Re_c = 3.28 \times 10^6$ (Fig. 4.11b); $\sigma = 0.148$ for $Re_c = 6 \times 10^6$ (Fig. 4.11c) . The normalized standard deviation, $\bar{\sigma}$, for the three Reynolds numbers, $Re_c = 1.64 \times 10^6$, 3.28×10^6, and 6×10^6 are 0.0192, 0.0248, and 0.0322, respectively.

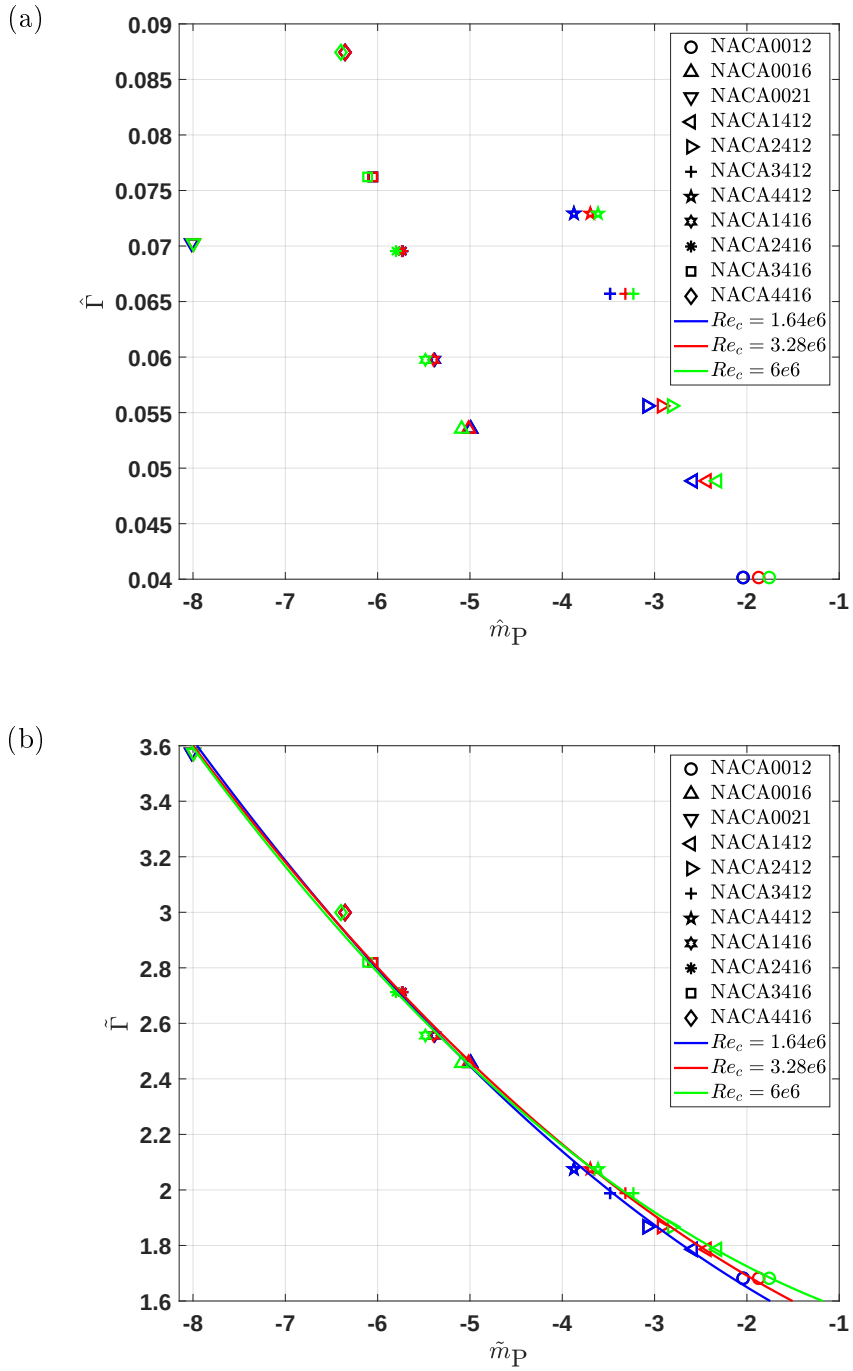

Figure 4.10: Data distribution of $\tilde{\Gamma}$ versus $\tilde{m}_{\mathrm{P}}$ for NACA1412 to NACA4412, NACA1416 to NACA4416, and NACA0021 at different Reynolds numbers: (a) $\hat{m}_{\mathrm{P}}$ vs $\hat{\Gamma}$, and (b) $\tilde{m}_{\mathrm{P}}$ vs $\tilde{\Gamma}$. The symbols used for each airfoil are chosen such that different symbols represent different airfoils, and the different colors represent different Reynolds number.

(a)

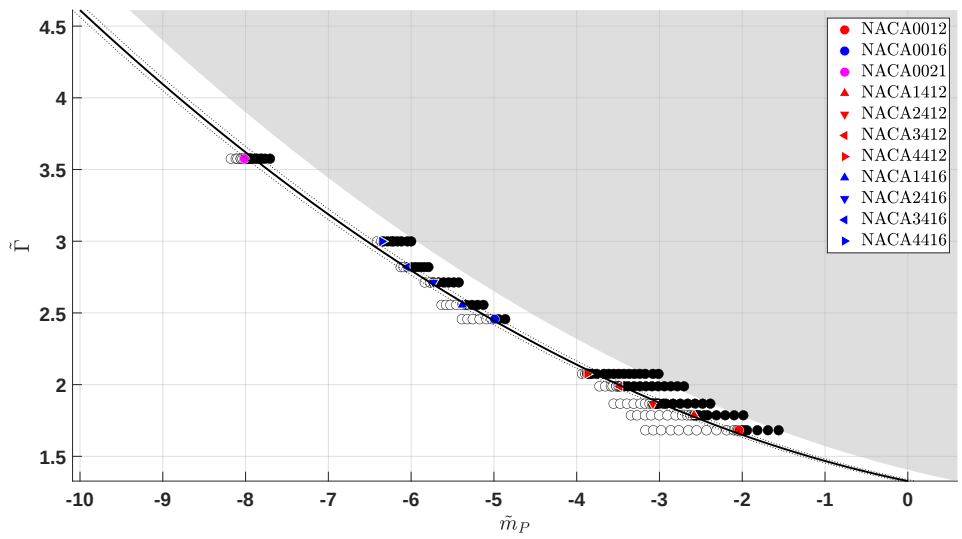
NACA0012
NACA0016
NACA0021
NACA1412
NACA2412
NACA3412
NACA4412
NACA1416
NACA2416
NACA3416
NACA4416
$\tilde{\Gamma}$
$\tilde{m}_P$

(b)

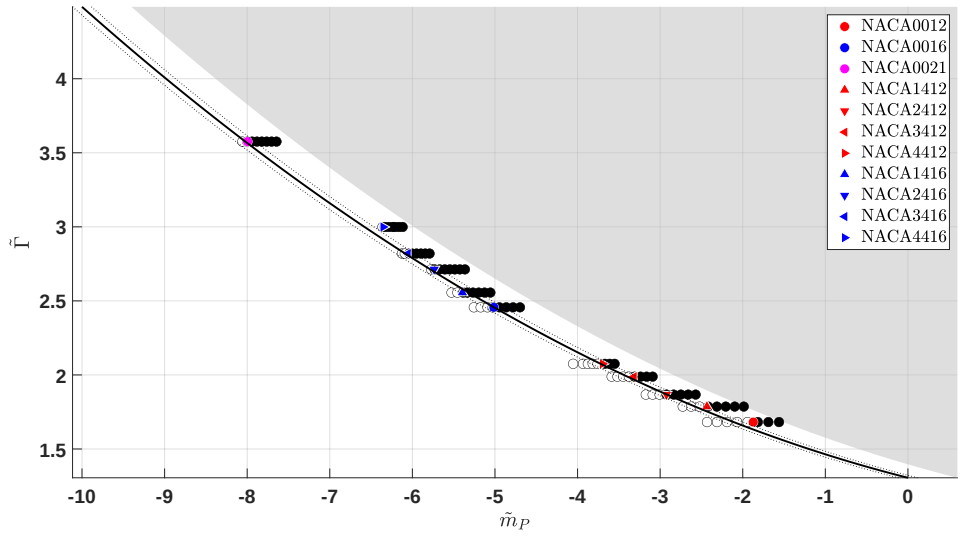
NACA0012
NACA0016
NACA0021
NACA1412
NACA2412
NACA3412
NACA4412
NACA1416
NACA2416
NACA3416
NACA4416
$\tilde{\Gamma}$
$\tilde{m}_P$

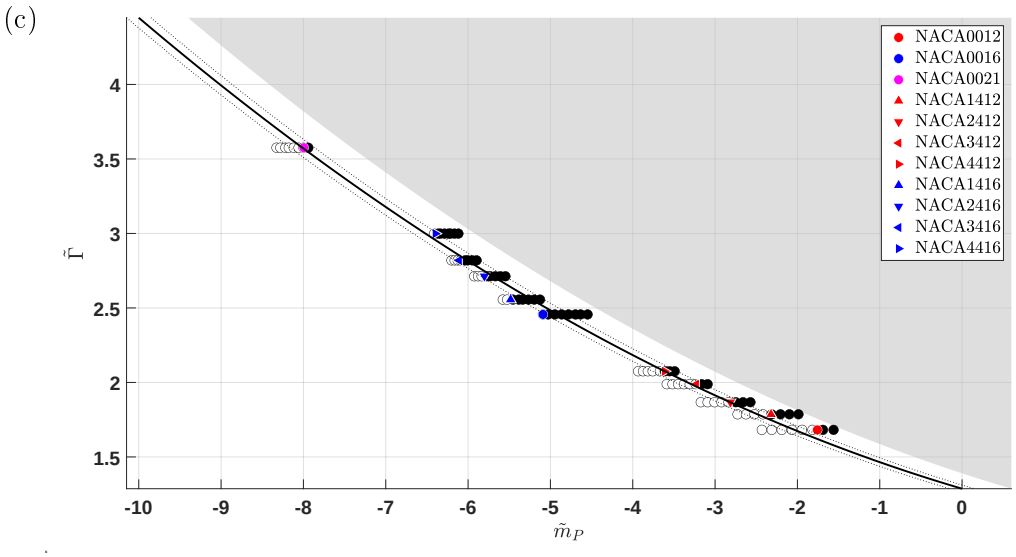

Figure 4.11: Law of incipient separation at different Reynolds numbers. (a) $Re_c = 1.64 \times 10^6$, (b) $Re_c = 3.28 \times 10^6$, and (c) $Re_c = 6 \times 10^6$. The data from the same airfoil lie on a horizontal line since $\tilde{\Gamma}$ is constant for a given airfoil. The colored symbols denote incipient separation ($C_{f_{\min}} = 0$), empty circles denote attached flow ($C_{f_{\min}} < 0$), and black circles denote separated flow ($C_{f_{\min}} > 0$). The solid black line is the data polynomial fit given by Eq. (4.7), and the dotted lines represent delineate a bandwidth of 2σ. The gray area indicates the RANS uncertainty region , i.e., the region in which the RANS prediction of $C_{f_{\min}}$ fails because of large separation.

Chapter 5

CONCLUSION

We have performed RANS simulations of two-dimensional turbulent flows over thirty-two NACA airfoils over a range of angles of attack at three different Reynolds numbers using the commercial CFD software ANSYS Fluent. First (Ch. 2), starting from the Thompson's method for grid generation [25], we developed an elliptic wall-normal grid generator, EWN-CGrid, which satisfies the property of grid-lines orthogonality within the boundary layer and at the airfoil's surface. EWN-CGrid allows grid points clustering at the L.E. and T.E. of the airfoil, as well, in the boundary layer and wake. For a given Reynolds number, the EWN-Cgrid can generate a mesh with the closest grid point to wall below $y^+_{\min} = 0.4$, allowing the use of RANS without any wall-function models to capture the flow in the viscous sublayer region. We have shown that EWN-CGrid considerably improves the quality of the grid with respect to the ANSYS Fluent structured grid as shown in Table. 2.1 and Figs. 2.3 and 2.4. Then (Ch. 3.1), we verified the convergence of RANS results with respect to domain size and grid resolution. Next (Ch. 3.2), we compared the results obtained using the RANS SA-RC [23] and SST-RC [18] models against the numerical results of the CFL3D code [7] and the experiments of Ladson [15]. Such analysis revealed better results for the SA-RC than the SST-RC model. Then (Ch. 3.2), we validated the RANS SA-RC model with the experiments of Wadcock [27] and established the range of fidelity of RANS. The pressure coefficient, C_p, profile over the NACA4412 airfoil for $0^\circ \leq \alpha \leq 14^\circ$ at $Re_c = 1.64 \times 10^6$ were compared with experimental measurements [27] and were found in good agreement within the range of attached flow and mild separation, i.e., including incipient separation, and the RANS results deviated from the experiments as the airfoil approached maximum lift (i.e., $\alpha \geq 12^\circ$). Finally (Ch. 4), we analyzed the effects of few key geometrical parameters of the airfoils,

angle of attack and Reynolds number on the incipiency of turbulent flow separation on the upper surface of the airfoil. The results showed the effect of changing airfoil thickness, h, and airfoil camber, h_c, is similar to that of changing airfoil angle of attack, α. As the airfoil angle of attack can have positive and negative values, we have used airfoil characteristic slope, m_{P}, that led us to formulate the law of incipient separation, Eq. (4.7), with the validity of the law demonstrated for $Re_c \in [1.64 \times 10^6, 6 \times 10^6]$.

The law of incipient separation over airfoils can be useful in aerodynamic design as a first-order approximation. The law requires the knowledge of only the geometrical features of the airfoil and the inflow Reynolds number, therefore, by knowing the airfoil profile, the flow can be kept attached to the airfoil's upper surface by limiting the value of $\tilde{m}_{\mathrm{P}}$ to be smaller than $\tilde{m}_{\mathrm{P}_{\mathrm{crit}}}$ for that airfoil. Further research via DNS and experiments will be necessary to provide more accurate coefficients for the law.

APPENDIX
GRID RANS RESULTS COMPARISON

RANS simulations on the Fluent grid and EWN-CGrid over a NACA4412 of $\alpha = 12°$ at $Re_c = 1.64 \times 10^6$ has been conducted and compared with Wadcock experimental measurements [27]. As shown in Fig. A.1, the C_f solution of the Fluent grid predicts separation near $x/c = 0.705$ while the experimental measurements suggest a separation point between $x/c = 0.815$ and 0.952. In Fig. A.1c, which plots the velocity profile at $x/c = 0.529$, the u/U_∞ profile can be seen deviating from the experimental results, conferring the earlier separation on the Fluent grid. For a quantitative analysis of the L_2 norm compared to the experimental measurements, with results shown in Table A.1, we find that for C_p, the Fluent grid has sightly better result, however, the solution of u/U_∞ shows that the Fluent grid deviates highly from experimental data.

σ of	C_p	u/U_∞	v/U_∞
Fluent grid	0.1216	0.1954	0.0034
EWN-CGrid	0.1342	0.0710	0.0090

Table A.1: L_2 norm of Fluent grid and EWN-CGrid compared with the experimental data of Wadcock [27] experimental data over a NACA4412 airfoil at $\alpha = 12°$, $Re_c = 1.64 \times 10^6$.

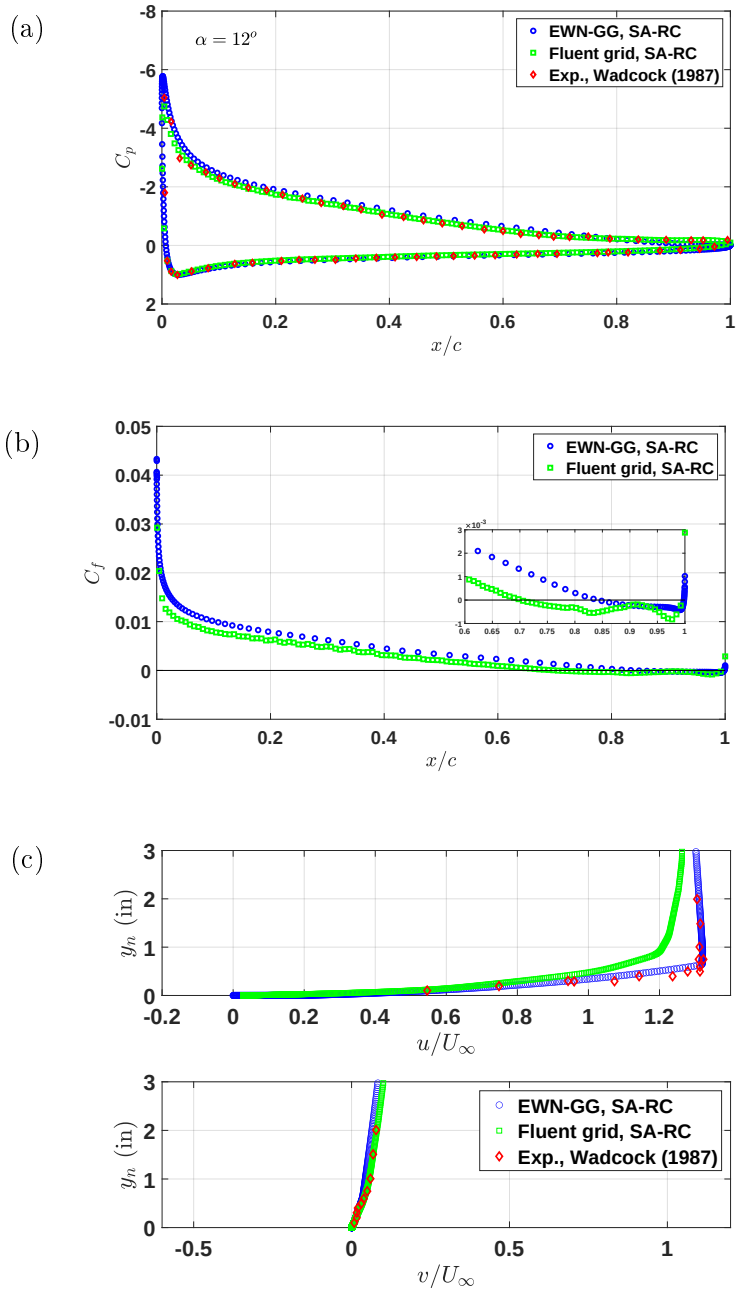

Figure A.1: Comparison of results obtained using the RANS SA-RC model with the ANSYS Fluent grid (green symbols), the EWN-CGrid (blue circles), and the experimental results of Wadcock [27] for the validation test-case of the turbulent flow over a NACA 4412 airfoil: (a) C_p, (b) C_f, and (c) velocity profiles at $x/c = 0.529$.

ANSYS FLUENT JOURNAL FILE USED FOR SIMULATIONS

In the present study, the journal file is used to automate a series of commands. The following file consists a journal case for RANS SA-RC on a NACA4412 at $\alpha = 12°$.

```
/file/read-case "naca4412_a0.cas.gz"
/file/read-data "naca4412_a0.dat.gz"

/define/models/viscous/spalart-allmaras yes
/define/models/viscous/curvature-correction? yes

/define/materials/change-create/air/air yes constant 1 no no yes
   constant 6.097e-7 no no no
/define/boundary-conditions/velocity-inlet/inlet yes yes no 1 no 0
    no 0.97814 no 0.20791 no no yes no 0.21044
/define/boundary-conditions/pressure-outlet/outlet yes no 0 no yes
    no no yes no 0.21044 yes no no

/report/reference-values/compute/velocity-inlet/inlet
/solve/set/p-v-coupling 24
/solve/set/gradient-scheme no no
/solve/set/discretization-scheme/nut 1
/solve/set/discretization-scheme/mom 1
/solve/set/discretization-scheme/pressure 12
/solve/set/high-order-term-relaxation/enable yes
```

```
/solve/set/high-order-term-relaxation/options/variables/select 2
/solve/set/high-order-term-relaxation/options/relaxation-factor 1
/solve/set/under-relaxation/body-force 1
/solve/set/under-relaxation/nut 0.95
/solve/set/under-relaxation/density 1
/solve/set/under-relaxation/turb-viscosity 1
/solve/set/limits 1 5e10 1e10

/solve/report-definitions/add/cd drag thread-names airfoil_low
   airfoil_up () q
/solve/report-definitions/edit/cd force-vector 0.97814 0.20791 q
/solve/report-definitions/add/cl lift thread-names airfoil_low
   airfoil_up () q
/solve/report-definitions/edit/cl force-vector -0.20791 0.97814 q

/solve/report-files/add/cd_file print yes report-defs cd () q
/solve/report-files/edit/cd_file file-name "cd_file" q
/solve/report-files/add/cl_file print yes report-defs cl () q
/solve/report-files/edit/cl_file file-name "cl_file" q

/solve/monitors/residual/convergence-criteria 1e-6 1e-6 1e-6 1e-6
/solve/initialize/compute-defaults/velocity-inlet/inlet
/solve/initialize/initialize-flow
/solve/set/number-of-iterations 10000
/solve/iterate
```

```
/file/export/tecplot/cpcf () pressure-coefficient skin-friction-
   coef q
/file/export/tecplot/vel_vor () x-velocity y-velocity velocity-
   magnitude vorticity-mag q
/file/export/tecplot/turb () viscosity-ratio viscosity-lam
   viscosity-eff viscosity-turb q
/file/export/ascii/velocity_pressure.dat () no pressure x-velocity
    y-velocity velocity-magnitude q no
/file/export/ascii/wall_data.dat airfoil_up airfoil_low () no
   velocity-magnitude pressure x-wall-shear y-wall-shear wall-
   shear skin-friction-coef pressure-coefficient q yes
/file/export/ascii/turb.dat () no viscosity-ratio viscosity-lam
   viscosity-eff viscosity-turb q no
/file/wcd "naca4412_re1_6e6_a12_sa_s.dat.gz"
```

GRID IMPORTATION OF FORTRAN GENERATED FILE

The EWN-CGrid used in the present study was implemented through Fortran. In order to run a Fluent simulation with an external grid, the format of the file needs to be changed from (.dat) to Plot3D (.grd). The Fortran code implementation for conversion of the 2-D grid into a Plot3D format is listed below.

```
nbl = 1
idim1 = imax ! # of grid pts in i
kdim = jmax ! # of grid pts in j

open (unit = 24, file='Mesh_for_Fluent.grd', action= 'write
    ', status='replace') ! Output file in format for Fluent
write (24,*) nbl
write (24,*) idim1(1),kdim(1)

write (24,*) ((x(i,j),i=1,idim1(1)),j=1,kdim(1)),&
((y(i,j),i=1,idim1(1)),j=1,kdim(1)) !write grid into
    plot3d format
close(24)
```

After reading the Plot3D file into Fluent, the boundary conditions needs to be assigned for the Fluent solver. The $i = 1$, $j = 1$, $i = N_i$, and $j = N_j$ will be the preassigned boundaries. Fluent reads the imported Plot3D grid into only two face zones, the “default_exterior-1” and the “default_interior-1”. The pre-defined face zones of “default_exterior-1” in the exterior will need to be separated into zones “inlet” and “outlet”. The separation of "Face Zones" in the Fluent application can be used to separated zones into “inlet” and “outlet”.

BIBLIOGRAPHY

[1] H. Abe, H. Kawamura, and Y. Matsuo. Direct numerical simulation of a fully developed turbulent channel flow with respect to the Reynolds number dependence. *Journal of Fluid Engineering*, 123(2):382–393, 2001.

[2] H. Arunkumar, C. Mangrulkar, and T. Gohil. Vortex dynamics and elliptical structure wake interaction in the proximity of wall using 2-d rans simulation. *MATEC Web of Conferences*, 144:04018, 01 2018.

[3] A. Bobke, R. Vinuesa, R. Örlü, and P. Schlatter. Large-eddy simulations of adverse pressure gradient turbulent boundary layers. *Journal of Physics: Conference Series*, 708:012012, 2016.

[4] M. S. H. Boutilier and S. Yarusevych. Separated shear layer transition over an airfoil at a low Reynolds number. *Physics of Fluids*, 24(8):084105, 2012.

[5] T. Cebeci, G. J. Mosinskis, and A. M. O. Smith. Calculation of Separation Points in Incompressible Turbulent Flows. *Journal of Aircraft*, 9(9):618–624, 1972.

[6] I. Celik, U. Ghia, P. Roache, and C. Freitas. Procedure for Estimation and Reporting of Uncertainty Due to Discretization in CFD Applications. *Journal of Fluids Engineering*, 130(7), 2008. 078001.

[7] NASA Langley Research Center. Turbulence modeling resource, 2021.

[8] D. Coles and A. J. Wadcock. Flying-Hot-wire Study of Flow Past an NACA4412 Airfoil at Maximum Lift. *AIAA Journal*, 17(4):321–329, 1979.

[9] J. N. N. Counsil and K. Goni Boulama. Low-Reynolds-Number Aerodynamic Performances of the NACA0012 and Selig–Donovan7003 Airfoils. *Journal of Aircraft*, 50(1):204–216, 2013.

[10] A. Ferrante and S. E. Elghobashi. A robust method for generating inflow conditions for direct simulations of spatially-developing turbulent boundary layers. *Journal of Computational Physics*, 198(1):372–387, 2004.

[11] C. Fletcher. *Computational Techniques for Fluid Dynamics 2*. Springer-Verlag Berlin Heidelberg, 1991.

[12] F. R. Goldschmied. An approach to turbulent incompressible separation under adverse pressure gradients. *Journal of Aircraft*, 2(2):108–115, 1965.

[13] M.R. Head. Entrainment in the turbulent boundary layer. *Aeronautical Research Council Reports and Memoranda*, 1958.

[14] Y. Khor and Q. Xiao. CFD simulations of the effects of fouling and antifouling. *Ocean Engineering*, 38(10):1065–1079, 2011.

[15] C. Ladson. *Effects of Independent Variation of Mach and Reynolds Numbers on the Low-speed Aerodynamic Characteristics of the NACA 0012 Airfoil Section*. NASA technical memorandum. National Aeronautics and Space Administration, Scientific and Technical Information Division, 1988.

[16] D. Lu, A. Aithal, and A. Ferrante. Law of Incipient Separation over Curved Ramps as Inferred by Reynolds-Averaged Navier–Stokes. *AIAA Journal*, 59(1):196–214, 2021.

[17] ANSYS Academic Research Mechanical, Release 18.0.

[18] F. Menter. Two-equation eddy-viscosity turbulence models for engineering applications. *AIAA Journal*, 32(8):1598–1605, 1994.

[19] P. Roache. *Verification and validation in computational science and engineering*, volume 895. Hermosa Albuquerque, NM, 1998.

[20] M. Samuell. *Development of a turbulent separated flow validation test case: Experimental and computational (RANS) studies*. Thesis, University of Washington, 2020.

[21] M. Shur, P. Spalart, M. Strelets, and A. Travin. Turbulence Modeling in Rotating and Curved Channels Assessing the Spalart Shur Correction. *AIAA Journal*, 38:784–792, 05 2000.

[22] F. Smirnov, P.and Menter. Sensitization of the SST Turbulence Model to Rotation and Curvature by Applying the Spalart Shur Correction Term. *Journal of Turbomachinery*, 131, 10 2009.

[23] P. Spalart and S. Allmaras. A one-equation turbulence model for aerodynamic flows. *AIAA*, 1992.

[24] B. S. Stratford. The prediction of separation of the turbulent boundary layer. *Journal of Fluid Mechanics*, 5(1):1 16, 1959.

[25] J. Thompson, B.K. Soni, and N.P. Weatherill. *Handbook of Grid Generation.* CRC Press, 1998.

[26] J. Thompson, F. Thames, and C. Mastin. Automatic numerical generation of body-fitted curvilinear coordinate system for field containing any number of arbitrary two-dimensional bodies. *Journal of Computational Physics*, 15(3):299–319, 1974.

[27] A. Wadcock. *Investigation of low-speed turbulent separated flow around airfoils* . National Aeronautics and Space Administration, Ames Research Center, 1987.